CATALYTIC ACTIVITY OF CERIA SURFACES STUDIED BY DENSITY FUNCTIONAL THEORY

DISSERTATION

zur Erlangung des akademischen Grades
Doctor rerum naturalium (Dr. rer. nat.)

im Fach Chemie

eingereicht an der

Mathematisch-Naturwissenschaftlichen Fakultät
der Humboldt-Universität zu Berlin

von

Herrn Dipl.-Chem. Thomas Erhard Kropp

Präsident der Humboldt-Universität zu Berlin
Prof. Dr. paed. Jan-Hendrik Olbertz

Dekan der Mathematisch-Naturwissenschaftlichen Fakultät
Prof. Dr. Elmar Kulke

Gutachter:
1. Prof. Dr. Joachim Sauer
2. Prof. Dr. Hans-Joachim Freund
3. Dr. Stefano Fabris

Tag der mündlichen Prüfung: 04.07.2016

ABSTRACT

Density functional theory is applied to study the catalytic properties of ceria surfaces with different terminations. Ceria is also used as a support material in heterogeneous catalysis to improve activity, selectivity, and stability of the active component. In this work, supported vanadia clusters are discussed. The oxidative dehydrogenation of methanol is used as a model reaction for C–H bond activation.

Ceria catalysts are often prepared in aqueous solution. As a result, the shape of ceria nanocrystallites depends on the relative stability of the different surface terminations in the presence of water. Furthermore, many reactions involve water either as a product, as a reagent, or as a solvent. Hence, water–surface interactions are studied as well.

Furthermore, the accuracy of three different functionals (B3LYP, HSE, and PBE+U) is assessed by comparison to experimental data such as barriers obtained via temperature-programmed desorption and infrared spectra.

Keywords: catalysis, ceria, density functional theory, methanol, oxidative dehydrogenation, oxides, surface science, and vanadia

ZUSAMMENFASSUNG

Unter Verwendung von Dichtefunktionaltheorie werden die katalytischen Eigenschaften von Cerdioxidoberflächen mit verschiedenen Terminierungen untersucht. Cerdioxid wird auch als Trägermaterial in der heterogenen Katalyse eingesetzt, um Aktivität, Selektivität und Stabilität der aktiven Komponente zu erhöhen. In dieser Arbeit werden geträgerte Vanadiumoxidcluster diskutiert. Dabei wird die oxidative Dehydrierung von Methanol als Modellreaktion zur Aktivierung von C-H-Bindungen genutzt.

Ceroxidpartikel werden oft in wässriger Lösung synthetisiert. Damit hängt die Form der Nanokristallite direkt von der relativen Stabilität der unterschiedlichen Terminierungen in der Gegenwart von Wasser ab. Außerdem ist Wasser an zahlreichen Reaktionen entweder als Produkt, Edukt oder Lösungsmittel beteiligt. Aus diesem Grund werden auch die Wasser-Oberflächenwechselwirkungen untersucht.

Des Weiteren wird die Genauigkeit von drei verschiedenen Funktionalen (B3LYP, HSE und PBE+U) durch den Vergleich mit experimentellen Daten evaluiert. Diese beinhalten Barrieren, die mittels Temperatur-programmierter Desorptionsspektroskopie erhalten wurden, und Schwingungsspektren.

Schlagwörter: Ceroxid, Dichtefunktionaltheorie, Katalyse, Methanol, Oberflächenchemie, oxidative Dehydrierung, Oxide und Vanadiumoxid

PUBLICATIONS

This thesis is based on the following publications:

1. Paier, J.; **Kropp, T.**; Penschke, C.; Sauer, J. Stability and Migration Barriers of Small Vanadium Oxide Clusters on the CeO_2(111) Surface Studied by Density Functional Theory. *Faraday Discuss.* **2013**, *162*, 233.

2. **Kropp, T.**; Paier, J. Reactions of Methanol with Pristine and Defective Ceria (111) Surfaces: A Comparison of Density Functionals. *J. Phys. Chem. C* **2014**, *118*, 23690.

3. **Kropp, T.**; Paier, J.; Sauer, J. Support Effect in Oxide Catalysis: Methanol Oxidation on Vanadia/Ceria. *J. Am. Chem. Soc.* **2014**, *136*, 14616.

4. **Kropp, T.**; Paier, J. Activity Versus Selectivity of the Methanol Oxidation at Ceria Surfaces: A Comparative First-Principles Study. *J. Phys. Chem. C* **2015**, 119, 23021.

5. Yang, C.; Bebensee, F.; Nefedov, A.; Wöll, C.; **Kropp, T.**; Komissarov, L.; Penschke, C.; Moerer, R.; Paier, J.; Sauer, J. Methanol Adsorption on Monocrystalline Ceria Surfaces. *J. Catal.* **2016**, 336, 116.

6. **Kropp, T.**; Paier, J.; Sauer, J. Interactions of Water with the (111) and (100) Surfaces of Ceria. **2016**, in preparation.

7. **Kropp, T.**; Paier, J.; Sauer, J. Selective Methanol Oxidation at Ceria-Supported Vanadia Oligomers. **2016**, in preparation.

CONTENTS

1. INTRODUCTION

1.1. MOTIVATION

Heterogeneous catalysis is an essential aspect of chemical technology, as numerous industrial processes are facilitated by catalysts. Solid catalysts are particularly attractive because they can be easily separated from liquid or gaseous products. Such catalysts are often comprised of an active component and a supporting oxide; both may affect the catalytic properties.[8,9]

Understanding the relationships between structure, composition, catalytic activity, and selectivity is the key issue in catalytic research. However, industrial catalysts are usually highly complex systems: To maximize the surface area, powder catalysts are employed, which typically have an ill-defined surface with many defective sites. To circumvent this complexity, well-defined model catalysts (e.g., ref 10) may be studied, and strategies have been proposed to overcome the materials gap between the simplified model and the real catalyst. Unlike industrial processes, such investigations are often carried out at low pressure leading to an additional pressure gap. Via a bottom-up approach, complexity can then be introduced step-wise.

Such model systems can be studied experimentally and theoretically, though understanding at the atomic level can only be achieved by combining both approaches. The discovery of the mechanism underlying the Haber–Bosch process marks one particularly successful application of this strategy, which culminated in the Nobel Prize for Gerhard Ertl.[11]

Compared to real working catalysts, gas phase clusters represent highly simplified model systems that can be used to study an isolated active site. Due to their limited size, gas phase models can be studied with high-level quantum chemical methods. In combination with experiments, this provides direct insight into reaction mechanisms and reactivity patterns (e.g., refs 10 and 12). However, the high degree of coordinative unsaturation may lead to a much higher reactivity of gas phase clusters compared with their condensed phase analogues.[12] Thus, it is important to consider the surroundings of the active site.

From an experimental point of view, the well-defined surfaces of single crystals and in particular thin films are attractive model systems as they can be studied with a wide array of surface techniques such as infrared (IR) spectroscopy, temperature-programmed desorption (TPD) spectroscopy, X-ray photoelectron spectroscopy (XPS), and scanning tunneling microscopy (STM) – just to name a few examples.[13]

However, surface models contain a large number of atoms, which require efficient quantum chemical methods such as Kohn–Sham density functional theory (KS-DFT).[14] Due to its low computational cost, DFT is frequently applied in condensed matter physics.[15] When applied under periodic boundary conditions, it can be used to simulate surfaces and bulk material. Wavefunction-based post-Hartree–Fock methods are currently limited to relatively small systems such as cluster models, though there is also a substantial effort to improve their scaling behavior (e.g., ref 16). Both approaches can be combined into a QM/QM method, where only a core region is treated with a rigorous quantum chemical method; its surroundings are treated with DFT.[17]

This work employs (generalized) KS-DFT to study the catalytic properties of different ceria (CeO_2) surfaces. These surfaces are computed under periodic boundary conditions and results are compared to experiments on thin films and nanocrystallites. From a computational perspective, proper electron localization into Ce f states poses a challenge to DFT.[18] Thus, different density functionals are tested and compared. Pristine and vanadia-decorated surfaces are studied to understand the cooperativity between ceria and vanadia that has been experimentally observed. In this context, the oxidative dehydrogenation (ODH) of methanol is used as a model reaction for C–H bond activation; this reaction may yield either formaldehyde or carbon oxides. Variations in activity and selectivity between different ceria surfaces are attributed to well-known concepts such as the degree of coordinative unsaturation, the reducibility, and the degree of reduction.[19]

1.2. CHEMICAL KINETICS

A catalyst transforms reactants into products via a repeated cycle of elementary steps. It participates in the reaction while being regenerated to its original form at the end of each cycle. However, chemical processes may lead to multiple products. The yield of a specific product divided by the overall conversion is called the selectivity toward that product. The activity of a catalyst is defined by the number of conversions per active site (or per surface area) in a given amount of time, i.e. the turnover frequency (TOF). The turnover number (TON) is the total number of conversions over the catalyst's lifetime and depends on its stability.[20]

The activity of a catalyst depends on the number of active sites, a concept that was introduced by Langmuir in 1915.[21] Typical active sites include coordinatively unsaturated ions as well as Lewis and Brønsted acids and bases. Experimentally, determining the number of active sites of a solid catalyst is challenging. IR spectroscopy in combination with probe molecules such as CO, methanol, pyridine, or water (e.g., refs 22 and 23) can provide an estimate, but the IR intensity is not necessarily proportional to the coverage. The surface area can be calculated using the Brunauer–Emmett–Teller (BET) method.[24]

The elementary steps of the reaction mechanism may include adsorption and desorption processes, diffusion, and chemical reactions. The principle of microscopic reversibility states that each step is reversible. The rate r of an elementary step (eq. 1) depends on the rate constant k, the thermodynamic activity a_i of each reactant, and the reaction order n_i for each reactant.

$$r = k \prod_i a_i^{n_i} \tag{1}$$

For an activated process, k can be calculated using the semiclassical Eyring–Polanyi equation

$$k = \kappa \frac{k_B T}{h} e^{-\frac{\Delta G^{\ddagger}}{k_B T}} \tag{2}$$

with the Planck constant h, the Boltzmann constant k_B, and the temperature T.[25] $\Delta G^{\ddagger}$ is the Gibbs free energy of activation. The transmission coefficient κ is often taken to be unity assuming that the transition state always proceeds to the product without any reverse reaction.[26]

A similar equation can be derived using the energy of activation $\Delta E^{\ddagger}$ (eq. 3), where thermal contributions are included through the microcanonical partition functions of reactants (q) and transition structure ($q^{\ddagger}$).

$$k = \kappa \frac{k_B T}{h} \frac{q^{\ddagger}}{q} e^{-\frac{\Delta E^{\ddagger}}{k_B T}} \tag{3}$$

This expression is very similar to the empirical Arrhenius equation with a pre-exponential factor that can be computed for any given temperature using the vibrational partition function, which may be calculated from the harmonic frequencies as discussed in Section 2.3.

As mentioned before, the semiclassical Eyring–Polanyi equation neglects quantum physical effects such as tunneling. To account for this, Wigner suggested a correction factor κ_w that depends on the frequency of the imaginary mode $\omega^{\ddagger}$ and the temperature (eq. 4).[27] For high temperatures and low imaginary frequencies, κ_w is close to unity, i.e. the semiclassical description. However, the expression rapidly diverges for low temperatures. Hence, other correction factors have been suggested (e.g., ref 28). Alternatively, non-adiabatic reactions such as electron or proton transfer reactions may be described using Marcus theory[29] or path integrals.[30]

$$\kappa_w(T) = \frac{\hbar\omega^{\ddagger}}{2k_B T} \sin^{-1}\left(\frac{\hbar\omega^{\ddagger}}{2k_B T}\right) \tag{4}$$

Once barriers and pre-exponential factors are known for each elementary step, it is possible to formulate a microkinetic model that can be used to calculate yield, selectivity, and TOF. Furthermore, it is possible to identify the rate-determining step and the relevant active site(s). However, this requires a tremendous amount of effort, which is why more efficient strategies are needed to screen large numbers of catalysts.

In the simplest case, catalytic activity correlates with readily measurable physical properties such as acidity, electronic structure, or hydrogenation as well as defect formation energies. These reactivity descriptors can be used to screen catalytic systems as recently discussed in ref 31. For example, oxygen defect formation energies can be used as a reactivity descriptor for

reactions that follow a Mars–van Krevelen mechanism [32] as demonstrated in refs 33 and 34. Thus, identifying and validating reactivity descriptors are pivotal tasks in catalytic research.

Alternatively, model reactions can be employed to screen for catalytic activity toward a specific type of reaction. The ODH of methanol to formaldehyde (eq. 5), for example, is used as a model reaction for C–H bond activation. At oxide surfaces, this reaction proceeds according to a Mars–van Krevelen mechanism with the following elementary steps: methanol adsorption, H transfer, product desorption, and a fast reoxidation step. The C–H bond breaking is the rate-determining step,[35,36] thus the intrinsic barrier of this oxidation step defines the catalytic activity.

$$CH_3OH + ½\ O_2 \rightarrow CH_2O + H_2O \quad (5)$$

In addition to activity and selectivity, accessibility and stability are important properties of a solid catalyst. The accessibility depends on the shape of the catalyst (powder, monolithic, etc.), which is beyond the scope of this work. However, it is an important aspect that needs to be considered for industrial application. The stability of a catalyst directly affects its life time, i.e. the number of iterations of the catalytic cycle that the catalyst can perform before deactivation. Various effects such as sintering and poisoning may deactivate a catalyst, which is why catalyst regeneration is often the key to success in practical heterogeneous catalysis.[20] Catalyst deactivation is also beyond the scope of this work, though thermodynamic stabilities will be discussed.

Ideally, a catalyst should be highly active with high selectivity and high stability over a wide range of temperatures, though low temperatures are desired to reduce energy consumption. Unfortunately, high activity is often accompanied by low selectivity. Therefore, tradeoffs are inevitable. It should also be mentioned that reaction engineering plays a crucial role in catalyst design. This work, however, focuses on the atomistic understanding of the relationship between structure, composition, activity, and selectivity of solid catalysts.

2. METHODS

2.1. DENSITY FUNCTIONAL THEORY

The description of many-electron systems is one of the most demanding problems in theoretical chemistry. Solving the Schrödinger equation requires approximations that, according to Dirac,[37] capture the "main features of complex atomic systems without too much computation." Such technical simplifications can affect the outcome of a calculation. Therefore, this chapter will briefly discuss the approximations underlying KS-DFT in order to understand the limitations of the method with a particular focus on extended systems.

The wavefunction Φ used in the non-relativistic, time-independent Schrödinger equation

$$\hat{\mathrm{H}}\Phi(r_i, R_A) = E_{tot}\Phi(r_i, R_A) \tag{6}$$

depends on the spatial coordinates of the *i*-th electron (r_i) and the *A*-th nucleus (R_A). Degrees of freedom (DOF) associated with the spin are omitted for clarity. In atomic units, the Hamiltonian $\hat{\mathrm{H}}$ for a system with *N* electrons and *M* nuclei reads

$$\hat{\mathrm{H}}(r_i, R_A) = -\sum_i \frac{1}{2}\nabla_i^2 - \sum_A \frac{1}{2}\nabla_A^2 - \sum_{i=1}^{N}\sum_{A=1}^{M}\frac{Z_A}{|r_i - R_A|} + \sum_{i=1}^{N}\sum_{j=1}^{N}\frac{1}{|r_i - r_j|} + \sum_{A=1}^{M}\sum_{B=1}^{M}\frac{Z_A Z_B}{|R_A - R_B|} \tag{7}$$

with Z_A being the charge of the *A*-th nucleus. The first two sums represent the kinetic energy of electrons and nuclei. The third sum describes the Coulomb attraction between electrons and nuclei; the remaining sums refer to the Coulomb repulsion between electrons and nuclei, respectively.

Ionic and electronic degrees of freedom can be decoupled using the Born–Oppenheimer approximation.[38] It is assumed that the cloud of electrons follows the nuclei adiabatically, which is justified by the large difference in mass. This is often combined with the adiabatic approximation, where the expansion of the wavefunction is restricted to a single electronic state, i.e. off-diagonal coupling is neglected. Such coupling terms are important for describing

interactions between multiple potential energy surfaces (PES) that occur e.g. in photochemical reactions.

Using the product ansatz $\Phi(r_i, R_A) = \Psi(r_i, R_A)\chi(R_A)$, where $\chi(R_A)$ is the ionic wavefunction and $\Psi(r_i, R_A)$ is the electronic wavefunction, the electronic Schrödinger equation (eq. 8) is obtained. The ionic coordinates are only a parameter for the electronic Schrödinger equation.

$$\hat{\mathrm{H}}_{el}\Psi(r_i, R_A) = E_{el}\Psi(r_i, R_A) \tag{8}$$

$$\hat{\mathrm{H}}_{el}(r_i, R_A) = -\sum_i \frac{1}{2}\nabla_i^2 - \sum_{i=1}^{N}\sum_{A=1}^{M}\frac{Z_A}{|r_i - R_A|} + \sum_{i=1}^{N}\sum_{j=1}^{N}\frac{1}{|r_i - r_j|} \tag{9}$$

Despite these approximations, eq. 8 becomes rapidly insoluble with system size as the electronic wavefunction depends on $3N$ coordinates. Simply storing the many-body wavefunction of small molecules such as N_2 is not feasible with current technology.

The Hartree–Fock (HF) ansatz approximates the many-electron Hamiltonian (eq. 9) with a sum of single-electron operators, called Fock operators $\hat{f}$. Slater determinants comprised of orthonormal spin orbitals $\psi_a(x_i)$, typically abbreviated with $\psi_a(i)$, are used as wavefunctions. Within molecular orbital theory,[39] each orbital is written as a linear combination of basis functions that form the basis set. Gaussian basis functions are frequently employed as they permit explicit integration of the Hamiltonian. However, these basis sets are not complete. Thus, convergence regarding the size of the basis set has to be ensured.

Energies and orbital coefficients are computed variationally using the Fock equations

$$\hat{f}(1)\psi_a(1) = \left[\hat{h}(1) + \sum_{b=1}^{N}\left(\hat{\mathcal{J}}_b(1) - \hat{\mathcal{K}}_b(1)\right)\right]\psi_a(1) = \sum_{b=1}^{N}\varepsilon_{ba}\psi_b(1) \tag{10}$$

with $a = 1, \ldots, N$. The Fock operator acting on the first electron in spin orbital ψ_a is equal to the sum of the Lagrange multipliers ε_{ba} times the spin orbitals ψ_b. The Fock operator itself consists of three parts: the single-electron Hamiltonian $\hat{h}$, the Coulomb operator $\hat{\mathcal{J}}_b$ (eq. 11), and the exchange operator $\hat{\mathcal{K}}_b$ (eq. 11). It should be noted that Coulomb and exchange contributions cancel out for $a = b$, i.e. spin orbitals do not interact with themselves.

$$\hat{J}_b(1)\,\psi_a(1) = \left[\int \psi_b^*(2)\frac{1}{|r_1 - r_2|}\psi_b(2)\,\mathrm{d}x_2\right]\psi_a(1) \tag{11}$$

$$\hat{\mathcal{K}}_b(1)\,\psi_a(1) = \left[\int \psi_b^*(2)\frac{1}{|r_1 - r_2|}\psi_a(2)\,\mathrm{d}x_2\right]\psi_b(1) \tag{12}$$

Since the Fock operator depends on all occupied spin orbitals, the Fock equations are solved self-consistently. The best possible solution obtained with this method is called the Hartree–Fock limit, which represents an upper limit for the electronic energy as the Hartree–Fock approach neglects, e.g., Coulomb correlation. Various post-Hartree–Fock methods have been developed to account for the missing correlation energy; notable examples include Møller–Plesset perturbation theory, coupled cluster, and multi-configuration self-consistent field. However, these methods are currently limited to relatively small system sizes due to the computational workload.

An alternative to this wavefunction-based formalism has been derived by Hohenberg and Kohn in 1964.[40] The corresponding Hohenberg–Kohn theorems state that every property of a quantum system is uniquely determined by the electron density $\rho(x) = |\Psi(x)|^2$ of the ground state. This approach uses a variational set of equations similar to eq. 10.

Within the Kohn–Sham approach,[14] a reference system is introduced that contains N non-interacting single-electron wavefunctions, i.e. Kohn–Sham orbitals. This reference system is chosen to match the electron density of the interacting system. The Coulomb energy can now be computed directly from the electron density, but the kinetic energy is derived from the Kohn–Sham orbitals. The remaining energy contributions are compiled in the exchange-correlation potential $v_{XC}[\rho]$, whose exact expression is unknown. However, $v_{XC}[\rho]$ does include correlation, which represents an improvement over the Hartree–Fock method.

There are many approximations for the exchange-correlation functional, that can be divided in the following categories: the local density approximation (LDA), the generalized gradient approximation (GGA), and hybrid functionals. The LDA exchange-correlation potential $v_{XC}^{LDA}(\rho)$ depends solely on the electron density,[14] which is only exact for the homogeneous electron gas.

GGA is still local, but the potential also depends on the gradient of the density to account for inhomogeneity. A parameter-free functional has been introduced by Perdew and Wang in 1991, hence PW91.[41] A modified version of PW91 has been developed by Perdew, Burke, and Ernzerhof, i.e. PBE.[42] In addition to the *ab initio* functionals, semiempirical exchange-correlation functionals have been developed by Becke (B88, ref 43) and Lee, Yang, and Parr (LYP, ref 44).

Because of the approximated exchange-correlation functionals, Coulomb and exchange interactions do not cancel out when using DFT. Thus, electrons interact with themselves, which is called the self-interaction error (SIE). Many shortcomings of DFT such as over-delocalization of electrons have been attributed to this artificial interaction, which is why there has been a substantial effort to develop methods that correct for SIE.

Hybrid functionals account for self-interaction by mixing DFT and Fock exchange. For example, the PBE0 hybrid functional mixes 75% PBE exchange with 25% Fock exchange.[45] Later, a range separation has been introduced to avoid calculating the slowly decaying long-range Fock exchange; the resulting hybrid functional is named after Heyd, Scuseria, and Ernzerhof (HSE, refs 46 and 47). B3LYP is another popular hybrid functional, which mixes B88 and Fock exchange with LYP and VWN correlation;[48,49] the mixing coefficients have been obtained by fitting to the G2 test set.

Calculating the Fock exchange for extended systems such as solids is computationally challenging. This can be avoided by using the computationally more efficient Hubbard U model Hamiltonian (cf. refs 50 and 51) that has been developed for Mott insulators. Based on the tight-binding model, it uses a modified Hamiltonian containing a repulsive potential U between sites that counteracts electron delocalization. While this improves the results obtained using GGA functionals, the HSE hybrid functional still outperforms PBE+U when applied to ceria, which is demonstrated in the following sections.

However, both GGA and conventional hybrid functionals lack a proper description of long-range dispersion interactions,[52] which affect adsorption processes. As a result, many researchers try to develop functionals that accurately account for dispersion.[53-57] This work will use the semiempirical C_6/R^6 terms developed by Grimme and coworkers, i.e. DFT+D2.[58]

2.2. Periodic Boundary Conditions

The methodology discussed so far can be used to compute isolated molecules as well as crystalline solids. In the latter case, periodic boundary conditions (PBC) can be applied to simulate bulk material leading to wavefunctions of the form

$$\psi_{n,k}(r) = u_{n,k}(r)\, e^{ikr} = \sum_{G} C_{n,k+G}\, e^{i(k+G)r}, \tag{13}$$

where $u_{n,k}(r)$ is the cell periodic part of the wavefunction obeying

$$u_{n,k}(r+\tau) = u_{n,k}(r). \tag{14}$$

τ can be any symmetry operation compliant with the crystal symmetry. Here, k is a wave vector that lies within the first Brillouin zone, G is a reciprocal lattice vector, and n represents the band index. $\psi_{n,k}(r)$ is a sum of Bloch functions and eq. 14 is known as Bloch's theorem.[59] The new quantum number k originates from the translational symmetry of the crystalline solid.

Eq. 13 can also be interpreted as a Fourier expansion in terms of plane waves at each k point, making plane waves a useful basis set under PBC. To increase computational efficiency, the series is truncated; a reasonable truncation criterion is the maximal kinetic energy of the plane waves, which can be easily calculated using

$$E_{kin} = \frac{\hbar^2}{2m}|k+G|^2 \tag{15}$$

with m being the electron mass. Only plane waves with a kinetic energy that does not exceed a given energy cutoff are considered. Unfortunately, the description of localized core states with high kinetic energy requires large energy cutoffs, i.e. a large number of plane waves in eq. 13. This is not feasible for extended systems.

Thus, the frozen core approximation is introduced, assuming that core states do not contribute to chemical bonds; core electrons only affect total energies by the average electrostatic potential in the vicinity of the core. Furthermore, the Coulomb potential is replaced by a soft pseudopotential with a finite value at the position of the nuclei.[60] This leads to nodeless

pseudo-wavefunctions that require significantly fewer terms in the Fourier expansion. This combined approach has been validated by von Barth and Gelatt.[61]

Modern *ab initio* pseudopotentials are generated self-consistently for isolated atoms.[62-65] The resulting pseudo-wavefunction (i) matches the true wavefunction outside a certain core radius, (ii) does not possess nodal planes, and (iii) has the same Kohn–Sham eigenvalues. The projector-augmented wave method (PAW) generalizes this concept by introducing projector functions localized within PAW spheres centered on the nuclei.[66,67] The plane wave expansions are determined by the overlap with these projector functions.

Furthermore, calculating the electronic potential of a Bloch function requires integrating over the Brillouin zone, which is typically approximated by a summation over a discrete amount of k points. Methods for selecting suitable sets of k points are discussed in refs 68-72. Total energies of insulators and semiconductors can be calculated with high accuracy using relatively few k points, but metals require a dense k mesh.

2.3. VIBRATIONAL PROPERTIES

The previous two chapters discuss methods for calculating the electronic energy of a given system. However, quantum mechanical systems fluctuate even at absolute zero, which results in zero-point energy (ZPE) contributions. To include some of the important temperature effects, entropies are required that can be calculated from the microcanonical partition function q. For example, ref 73 discusses the importance of adsorption entropies. This section briefly outlines the calculation of these properties from harmonic frequencies.

Within the harmonic approximation, the PES is estimated with a second-order polynomial around the equilibrium structure for each decoupled vibrational DOF. This leads to equally spaced energy levels (eq. 16) for each harmonic oscillator, which depend on the angular frequency ω_i. Zero-point vibrational energies (ZPVE) are obtained for $n = 0$.

$$\varepsilon_{n,i} = \frac{\hbar\omega_i}{2}(2n+1) \tag{16}$$

The angular frequencies ω_i are obtained by diagonalizing the mass-weighted matrix of second derivatives of the total energy, i.e. the Hessian matrix; each eigenvalue λ_i translates into an angular frequency via $\omega_i^2 = \lambda_i$. If the analytical dependence of the potential on the atomic positions is unknown, these derivatives can be computed numerically using finite differences.

Harmonic frequencies systematically overestimate fundamental frequencies. Anharmonicities may be included with higher-order force constants, which is very expensive for extended systems. Scaling factors obtained by fitting harmonic frequencies to fundamentals represent a more economic approach (e.g., ref 74). Such scaling factors also account for systemic errors that stem from the electronic structure method. For example, the gradient-corrected PBE functional underestimates frequencies. Thus, harmonic PBE frequencies tend to be close to experimental values due to a favorable error cancellation.[74] IR intensities depend on the derivative of the dipole moment along the normal mode and can be calculated as described in ref 75.

Alternatively, molecular dynamics (MD) simulations can be used to compute vibrational properties of a system. Here, the motion of the atoms is calculated using Newtonian mechanics. To account for zero-point motion as well as violations of the detailed balance resulting from the classical treatment, quantum correction factors may be employed.[76,77] The IR spectrum can then be obtained as the Fourier transformation of the autocorrelation function of the dipole moment; thermodynamic properties can be computed via umbrella sampling[78] or thermodynamic integration[79] as applied in ref 80.

To increase computational efficiency, MD simulations often employ force fields, which are seldom reliable enough to describe molecule–surface interactions accurately. Thus, *ab initio* MD simulations using DFT are performed instead.

Assuming a Boltzmann distribution, the molecular partition function q can be computed using eq. 17 with $1/\beta = k_b T$. For the harmonic oscillator, ε_i is linear with i (eq. 16), which greatly simplifies the expression of the partition function.

$$q = \sum_i e^{-\beta \varepsilon_i} \tag{17}$$

By multiplying the partition functions for each vibrational DOF, one obtains

$$q_{vib} = \prod_i \frac{\mathrm{e}^{-0.5\beta\hbar\omega_i}}{1-\mathrm{e}^{-\beta\hbar\omega_i}} \ . \tag{18}$$

For isolated molecules, translational and rotational degrees of freedom have to be included as well. The translational partition function q_{trans} of an ideal particle in a box depends on its mass m, the pressure P, and the temperature (eq. 19); the rotational partition function of a rigid polyatomic rotor q_{rot} depends on the temperature and moment of inertia I for each rotation axis (eq. 20). A thorough derivation of these partition functions can be found in ref 25.

$$q_{trans} = \left(\frac{2\pi m}{\beta h^2}\right)^{1.5} \frac{1}{\beta P} \tag{19}$$

$$q_{rot} = \left(\frac{8\pi}{\beta h^2}\right)^{1.5} \sqrt{I_x I_y I_z} \tag{20}$$

The entropy of a given system can then be calculated using $S = \frac{\partial}{\partial T} k_B T \ \sum \ln(q_i)$.

2.4. Optimization of Transition Structures

Within the framework of transition state theory, reaction kinetics are derived from stationary points on the PES. Each stable structure is represented by a (local) minimum. Thus, all eigenfrequencies are real. Neighboring minima are connected through a minimum energy pathway or intrinsic reaction coordinate (IRC), that encompass a first-order saddle point (one imaginary eigenfrequency $\omega^{\ddagger}$), i.e. the transition structure (TS). The eigenvector corresponding to $\omega^{\ddagger}$ is a tangent to the IRC at the transition structure.[81]

Eigenvector following is a straightforward transition structure optimization algorithm.[82] Starting with an initial guess close to the TS, the energy is maximized along the eigenvector with the most negative eigenvalue, i.e. the IRC; the remaining degrees of freedom are minimized normally. Instead of recalculating the Hessian matrix for every step, many implementations (e.g., ref 83) use updating schemes. Nevertheless, this algorithm cannot be directly applied to extended systems due to the poor scaling behavior of the evaluation of the Hessian matrix.

Henkelman and Jónsson [84] introduced a comparable method that does not require Hessian matrices. They use two replicas of the system with a constant displacement, hence the name dimer method. This dimer is rotated to minimize the total energy of the system, which is equivalent to finding the lowest curvature at this point of the PES. Then the dimer is translated to maximize the energy along the displacement vector while minimizing the energy for all orthogonal degrees of freedom. Ref 85 shows that an improved dimer method (IDM) outperforms Baker's implementation [83] of eigenvector following.

Mousseau and coworkers [86] have implemented another eigenvector following technique that uses the Lanczos algorithm to find the most negative eigenvalue without calculating the entire Hessian matrix. Regardless of their differences, these uphill walking algorithms require an initial guess for the TS that has to be provided by chemical intuition or other TS search algorithms.

The synchronous transit method [87] represents one of the earliest interpolation methods. It searches for the maximum in energy along a linear (LST) or parabolic (QST) trajectory connecting reactant and product structure. The results of a QST calculation can be used as an initial guess for eigenvector following algorithms as implemented by Schlegel and coworkers.[88,89]

The nudged elastic bands (NEB) method [90,91] models the minimum energy pathway between reactant and product with a series of structures called images. Each image is optimized simultaneously, while neighboring ones are connected with harmonic spring forces. This penalty function prevents the optimizations from converging into local minima. In contrast to the synchronous transit method, this approach does not limit the shape of the minimum energy pathway. The climbing image method [92] removes the penalty function for the structure with the highest energy. Instead, its energy is maximized along the trajectory. Hence, the image converges to a saddle point.

The string method [93,94] is another chain of states method for obtaining minimum energy pathways. Instead of adding an artificial spring force, a Lagrange multiplier term is added to enforce predefined properties of the spline connecting neighboring images (see ref 93 for more

details). The string method can be considered a generalization of the NEB method. The growing string method [95] was later introduced to eliminate the need for an initial guess.

Other algorithms rely on penalty functions to find transition structures connecting reactants with unknown product structures. Notable examples include metadynamics [96] and the artificial force-induced reaction method.[97] These methods can be used to generate reaction networks automatically.[98] Starting with a single minimum energy structure, transition structures are generated that connect this minimum with neighboring minima. This procedure is then repeated for each new minimum energy structure. While this approach completely removes the need for an initial guess, it is currently limited to relatively small systems due to the tremendous computational cost.[99-101]

2.5. Computational Details

Calculations were performed using the PAW method (cf. section 2.2) as implemented in the Vienna *ab initio* simulation package (VASP).[102,103] A plane wave kinetic energy cutoff of 600 eV was used and structure optimizations were performed until forces acting on relaxed atoms were below 0.02 eV/Å. Dipole moments perpendicular to the surface were corrected with the approach presented in ref 104.

Unless stated otherwise, the PBE exchange–correlation functional [42] is used with an effective Hubbard-type U parameter of 4.5 eV for the Ce 4*f* states, i.e. PBE+U (cf. ref 105). The specific implementation follows Dudarev et al.[106,107] Selected structures were also calculated using the hybrid functionals B3LYP [44,48] and HSE.[46] Structures optimized using PBE were proven to be minima by the absence of imaginary frequencies.

Harmonic frequencies and normal modes were obtained by finite differences of the gradients with displacements of 0.015 Å (central differences). Frequency calculations include all adatoms and the topmost three atomic layers. Thermodynamic properties were calculated using the equations presented in section 2.3 as implemented in the THERMO package by GiovanniMaria Piccini.[108]

The semiempirical C_6/R^6 term by Grimme and coworkers [58] was added to correct for missing long-range dispersion-type interactions, i.e. DFT+D2. Required parameters for Ce were taken from ref 109. The global scaling parameters are 0.75 (PBE), 1.05 (B3LYP), and 0.6 (HSE).

Transition structures were obtained by NEB calculations [90,91] in combination with the climbing image method.[92] These calculations typically use eight images and a spring constant of 5 eV/Å^2. The improved dimer method was used to refine these structures.[84,85]

3. SYSTEMS OF INTEREST

Cerium dioxide (ceria) represents a very active oxidation catalyst and is therefore widely employed in heterogeneous catalysis.[110,111] Due to its exceptional oxygen storage capacity, ceria is used for exhaust catalysis,[112] solid oxide fuel cells,[113] and self-cleaning domestic ovens.[114] This high activity stems from low oxygen defect formation energies and accessible Ce *4f* states, which become occupied by excess electrons once an overall electroneutral oxygen vacancy is formed.[115] Occupation of Ce *4f* states leads to the formation of atom-like split-off states in the band gap.[105] Re-oxidation of Ce^{3+} to Ce^{4+} is similarly easy.

Ceria has the fluorite structure (space group $Fm\bar{3}m$) with a lattice constant of 541 pm,[116,117] and the thermodynamically stable low-index surfaces with (111), (110), and (100) orientation (cf. Figure 1) have been comprehensively studied using computational and experimental approaches as recently discussed in refs 18 and 118, respectively.

DFT predicts an increase in surface energies according to (111) < (110) < (100), and surface properties vary drastically with the orientation.[119-121] Furthermore, defects and coordinatively unsaturated sites such as steps, kinks, and corners are strongly involved in the surface chemistry of ceria.[122] In addition to pristine ceria surfaces, vanadia-decorated surfaces will be discussed in this work as ceria may also be used as a support material in heterogeneous catalysis. Unlike other support materials such as silica or alumina, the reducible ceria increases the activity of supported vanadia clusters as shown in refs 3 and 123.

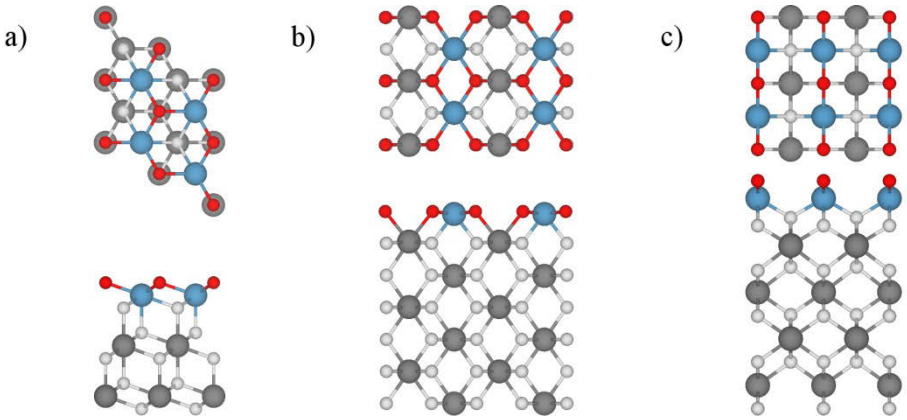

Figure 1: Top and side views on *p*(2×2) ceria (111), (110), and (100) surface models. VESTA[124] has been used for visualizing structural models using the following color code: Ce (dark gray; surface blue), O (light gray; surface red).

Recently, it was shown that rare earth elements such as cerium are also essential cofactors in the methanol dehydrogenase of *Methylacidiphilum fumariolicum* SolV, which has been isolated from volcanic mudpots near Naples.[125]

3.1. Ceria (111) Surfaces

As shown in Figure 1a, a slab model exposing this surface consists of O–Ce–O trilayers. Surface O ions are coordinated by three Ce ions, whereas subsurface O ions have the same coordination number (CN) as bulk oxygen (CN = 4). Surface Ce ions are coordinated by seven anions. According to DFT, this is the most stable surface termination with negligible relaxation contributions to the surface energy as shown in Table 1. Thus, it is not surprising that (111) is also the most thoroughly investigated surface orientation as recently discussed by Mullins.[118]

Defect formation energies for surface and subsurface oxygen vacancies in the (111) surface obtained using DFT are similar,[126] but they strongly depend on the Ce^{3+} localization pattern.[18] PBE+U underestimates the defect formation energy compared to HSE, though both values are lower than experimentally observed defect formation energies.[111]

Experimentally, the degree of reduction can be determined from Ce 3*d* photoemission spectra obtained using XPS.[127] Furthermore, CO can distinguish between Ce^{4+} and Ce^{3+} as its C–O stretching band is red-shifted upon adsorbing at Ce^{3+} sites compared to Ce^{4+} sites. Thus CO

Table 1: Surface energies as well as surface oxygen defect formation energies for ceria surfaces obtained with different density functionals (cf. Section 2.1). Defect formation energies for bulk ceria are stated for comparison. Adapted with permission from ref 4. Copyright 2015 by the American Chemical Society.

	Surface energy [J/m^2]			Defect formation [eV]		
	Unrelaxed	Relaxed	Δ_{relax}	Unrelaxed	Relaxed	Δ_{relax}
(100), PW91+U	2.05 [a]	1.41 [a]	-0.64 [a]	-	2.27 [b]	-
(100), PBE+U	2.15	1.44	-0.71	2.39	1.28	-1.11
(100), HSE	2.60	1.72	-0.88	2.70	1.56	-1.14
(110), PW91+U	1.25 [a]	1.05 [a]	-0.20 [a]	-	1.99 [b]	-
(111), PBE+U	0.69	0.68	-0.01	3.80 [c]	1.84 [c]	-1.96 [c]
(111), HSE	-	0.81 [d]	-	4.44	2.44	-2.00
Bulk, PBE+U [e]				4.22	2.76	-1.46
Bulk, HSE [e]				4.96	3.78	-1.18
Obsd.[f]					4.0 ± 0.1	

[a] Ref 119; [b] ref 128; [c] ref 109; [d] ref 129; [e] values refer to a $Ce_{32}O_{64}$ supercell; [f] ref 111.

can be used as an IR probe.[127] Ce^{3+} sites also bind Au atoms more strongly.[130] Therefore, Ce^{3+} ions can be detected using STM after depositing Au atoms at ceria surfaces.

Ceria (111) surfaces expose hexagonal nanoislands that are comprised of two different types of step edges.[131-134] The more stable type 1 step edges resemble one-dimensional (110) facets, while the less stable type 2 step edges resemble (100) facets.[133] Oxygen defect formation energies for step edge sites are lower than for (111) terraces.[135]

3.2. CERIA (100) SURFACES

Conventionally employed models for this ceria surface are oxygen-terminated (cf. Figure 1c), though characterizations of the (100) surface have not been definitive.[136-142] Due to its inherent polarity, mechanisms are required that compensate for the surface dipole moment.[143-145] This results in large relaxation contributions to the surface energy (cf. Table 1). Ref 120 has suggested that ceria (100) might feature a variety of terminations in constant flux rather than a "static" one. (100) is also the least stable surface orientation,[119-121] which corresponds with the lowest coordination numbers in the surface layer, i.e. CN = 2 (6) for oxygen (cerium) ions.

Oxygen defect formation energies for ceria (100) are significantly smaller than for ceria (111) as shown in Table 1 indicating higher activity for oxidation reactions following a Mars–van Krevelen mechanism. Defects in surface position are highly favored over defects in subsurface position.[4] In fact, the subsurface defect formation energy at the (100) surface (3.13 eV, PBE+U) is even larger than the bulk defect formation energy (2.76 eV, PBE+U). The stronger binding of the subsurface oxygen atom in the (100) surface is due to electrostatic interaction as reflected by a lower Madelung potential at the subsurface vacancy (-2.3 V) compared with the surface vacancy (±0.0 V). For ceria (111), the Madelung potential at the surface vacancy (-1.7 V) is lower than at the subsurface vacancy (-1.2 V) due to relaxation.[126]

3.3. VANADIA-DECORATED CERIA SURFACES

As recently demonstrated by experimental and theoretical studies on model catalysts,[123,146-148] ceria stabilizes vanadium in its highest oxidation state, i.e. V^{5+}, by accommodating electrons in the cerium *f* states. Such a redox participation of the surroundings of an active M=O site has also been found in enzymes and points to a unifying concept in catalysis. For example, cytochrome P450 selectively oxidizes C–H bonds to C–OH bonds. Its active site is an Fe^{IV}=O species surrounded by a porphyrin ligand that also participates in the redox reaction.[149]

While the higher activity of ceria-supported catalysts compared to non-reducible supports such as alumina and silica has been rationalized [123,148] using the energy of oxygen defect formation as a descriptor,[33,150] detailed information on how the support interferes with the elementary reaction steps is still missing.

Freund and coworkers [146] have shown that vanadium deposition on ceria (111) leads to vanadyl-terminated O=VO_3 species. XPS of these samples have revealed a Ce 4*f* peak, indicating vanadium in its highest oxidation state (+5), which is supported by DFT.[151,152] The nuclearity of these vanadia species, which sinter into larger polymers upon annealing to 700 K, can be directly observed by STM. Ref 109 discusses the stability of various vanadia oligomers (up to V_3O_6), and the corresponding phase diagram is shown in Figure 2. Vanadia trimers were found to be the

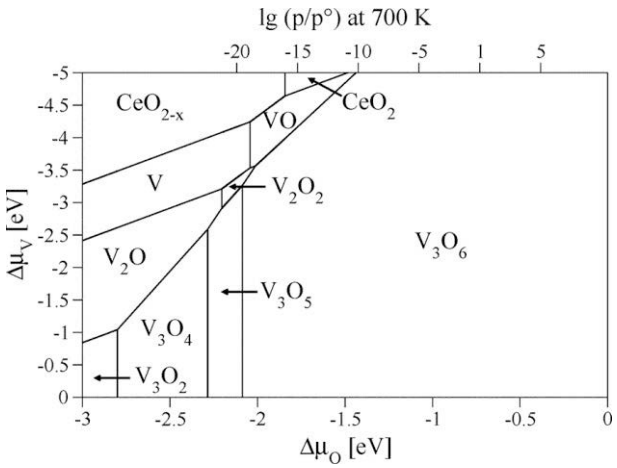

Figure 2: Phase diagram of various vanadia clusters on the ceria (111) surface as a function of $\Delta\mu_V$ and $\Delta\mu_O$. The chemical potential of oxygen has been translated into a pressure scale at 700 K. Reprinted with permission from ref 109. Copyright 2013 by the American Chemical Society.

most stable clusters, but oligomerization only occurs at high temperatures since the migration of vanadia clusters along the (111) surface is kinetically hindered.[1]

VO_2 is the most stable vanadia monomer on the ceria (111) surface under the slightly reducing conditions of the model catalyst experiment in ref 146. Vanadium is stabilized in its +5 oxidation state, and one electron is transferred into the Ce *f* states as indicated by XPS and DFT+U.[146] As shown in Figure 3b, this structure features a cavity in the ceria surface that will be referred to as pseudovacancy (cf. ref 1). This oxygen spill-over from ceria to vanadia is driven by the strong preference of vanadium for a tetrahedral coordination. The oxygen defect formation energy at the VO_2 monomer is particularly low (0.84 eV, PBE+U) indicating high catalytic activity.[109]

The corresponding trimer (V_3O_6 as shown in Figure 3c) is thermodynamically favored at this

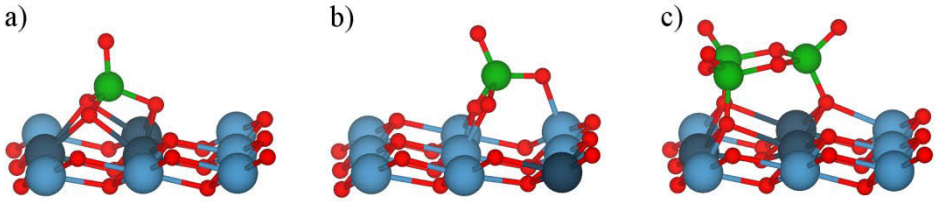

Figure 3: Side views on ceria-supported VO (a), VO_2 (b), and V_3O_6 (c) using the following color code: Ce^{3+} (dark blue), Ce^{4+} (blue), O (red) and V (green). This color scheme will be used throughout this work.

surface with a trimerization energy of -162 kJ/mol.[109] After annealing catalysts with vanadia loadings of up to 5.5 V/nm^2 to 700 K, the trimer is the most abundant vanadia species at this surface.[146] Structural details of this structure are discussed in refs 1 and 109: three VO_2 units form a six-membered ring and the three Ce^{3+} ions that are formed upon vanadia deposition localize beneath this ring. The oxygen defect formation energy at the trimer (2.09 eV, PBE+U) is slightly higher than at the pristine surface (1.84 eV, PBE+U),[109] which can be rationalized with the higher degree of surface reduction.

4. Results and Discussions

4.1. Methanol Adsorption at Ceria Surfaces

Previous theoretical studies (refs 153 and 154) considered monomeric methanol adsorption structures at pristine and oxygen-defective ceria (111) surfaces. The results could not explain the complex IR patterns in the CO stretching region of methanol at polycrystalline ceria,[155-157] thin films,[158-162] and supported nanoparticles.[162]

To assign the observed features, ref 5 combines IR experiments at single crystals with an extensive DFT investigation studying various adsorption structures at different methanol coverage. The resulting assignment is given in Table 2.

In 1997, Badri et al.[156] assigned the observed IR peaks *ad hoc* to methoxide species differing by the number of coordinated Ce ions, i.e. monodentate (= atop), bidentate (= bridging), and tridentate methoxide species. Since then, their assignment has been used throughout the literature. However, Table 2 shows that H bonds also affect CO stretching modes.

This can be rationalized using the concept of Pauling bond strength.[163] The CO stretching wavenumber of an isolated methoxide anion is 1130 cm^{-1} (PBE in ref 5). Each cation coordinated to the methoxide weakens the C–O bond leading to a redshift for the corresponding CO stretching mode. This redshift depends on the charge of the cation and the bond length.

Table 2: Assignment of experimentally observed wavenumbers $\tilde{\upsilon}_{Obsd.}$ (cm^{-1}) to CO stretching modes of different methanol adsorption structures (coordinating cations are given in parentheses). Adapted with permission from ref 5. Copyright 2016 by Elsevier.

$\tilde{\upsilon}_{Obsd.}$	Assignment	Also observed for …
1108 (±0)	(Ce)–**O**–CH_3	nanoparticles: 1104 cm^{-1} (ref 157); polycrystallites: 1103 cm^{-1} (ref 155), 1108 cm^{-1} (ref 156); thin films: 1105 cm^{-1} (ref 158), 1104 cm^{-1} (ref 162)
1085 (-23)	(Ce, H)–**O**–CH_3	nanoparticles: 1077 cm^{-1} (ref 157); thin films: 1080 cm^{-1} (ref 147)
1060 (-48)	(Ce, 2H)–**O**–CH_3	polycrystallites: 1050 cm^{-1} (ref 155), 1065 cm^{-1} (ref 156); thin films: 1058 cm^{-1} (ref 158)
1037 (-71)	(Ce)–**HO**–CH_3 (2Ce)–**O**–CH_3	nanoparticles: 1037 cm^{-1} (ref 157); polycrystallites: 1031 cm^{-1} (ref 155), 1042 cm^{-1} (ref 156); thin films: 1038 cm^{-1} (ref 162)
	(3Ce)–**O**–CH_3	nanoparticles: 1016 cm^{-1} (ref 157); polycrystallites: 1015 cm^{-1} (ref 156); thin films: 1027 cm^{-1} (ref 158)

Therefore, the degree of surface reduction (Ce^{3+} instead of Ce^{4+}) affects the IR spectrum just like the strength of H bonds. This is illustrated in Figure 4.

With increasing methanol coverage, dimers consisting of one molecular methanol species and a hydrogen-bonded methoxide form at the ceria (111) surface (cf. ref 5). The C–O bonds of both species couple via the H bond introducing an additional shift of the CO stretching wavenumber. This shows that a simple relation between the redshift of the methoxy CO stretching mode and the number of Ce cations coordinated to the methoxide (as often used in previous work) does not apply.

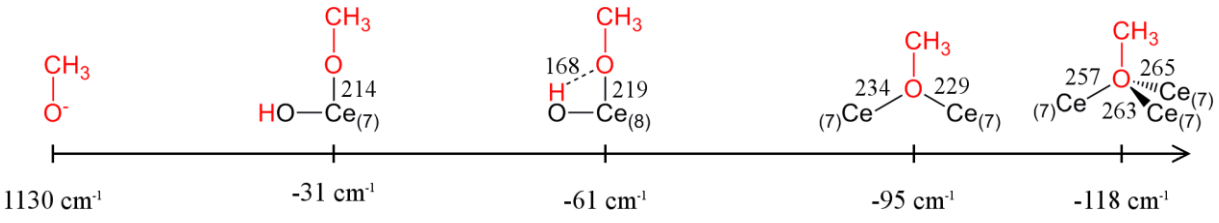

Figure 4: Dissociative methanol adsorption structures along with the corresponding redshift of the CO stretching mode relative to the gas phase methoxy anion obtained with dispersion-corrected PBE+U. Atoms originating from methanol are red; and coordination numbers are given in parentheses. Bond lengths are given in pm.

The following assignment was derived in ref 5. Methanol adsorption at the ceria (110) surface yields a sharp IR signal at 1108 cm^{-1}. This is in agreement with the assignment by Mullins and coworkers.[157] Interestingly, this IR band is also observed for ceria (111) films.[147,158,162] This can be attributed to methanol adsorption at step edges resembling (110) facets (cf. ref 133). Methanol adsorption at these step edges is significantly more exothermic (-1.31 eV, dispersion-corrected PBE+U) than at the pristine surface (-0.91 eV). Thus, the IR band corresponding to step edges is expected to be visible even at low coverage.

Bridging methoxide species were obtained at (100) facets and step edges resembling (100) facets. The corresponding CO stretching mode is predicted to occur at 1035 cm^{-1} (dispersion-corrected PBE+U), which is close to the CO stretching mode of molecularly adsorbed methanol (1037 cm^{-1}).[5] It is therefore not possible to easily distinguish between both species, though molecular adsorption is thermodynamically less favored at low coverage.

Tridentate methoxide species may form upon methanol adsorption into surface oxygen vacancies in the ceria (111) surface as previously described in ref 154 leading to IR bands at ca. 1020 cm^{-1}. Methanol adsorption at these surface defects is highly exothermic (-2.39 eV, dispersion-corrected PBE+U).

At the pristine (111) surface, CO stretching modes occur between 1085 and 1060 cm^{-1} depending on the methanol coverage. The computed IR spectrum of a methanol monolayer is shown in Figure 5. When using deuterated methanol, CD bending modes occur in the CO stretching region as well. Thus, methanol is a suitable surface probe for characterizing ceria surfaces as suggested in refs 23 and 164.

The results of this investigation can also be used to discuss the accuracy of computational frequencies. Ref 5 compares experimentally observed fundamentals, harmonic frequencies obtained using PBE+U, and the results of an *ab initio* MD simulation.

The harmonic frequencies were calculated numerically, and a numerical error of ±10 cm^{-1} in absolute wavenumbers has been estimated. The value of the displacement for the finite differences as well as the choice of the coordinate system have the biggest impact on the

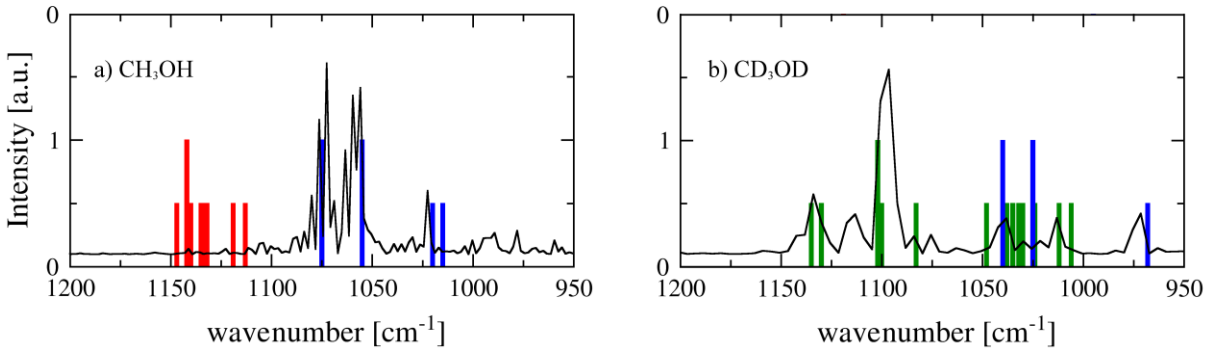

Figure 5: Harmonic vibrational spectra of CH_3OH (a) and CD_3OD (b) monolayers adsorbed at pristine ceria (111) using the following color code: red (methoxy rocking modes), blue (CO stretching modes), and green (CD bending modes). The results of MD simulations are shown as a black line. Adapted with permission from ref 5. Copyright 2016 by Elsevier.

wavenumber. On average, harmonic frequencies obtained with PBE+U underestimate experimental fundamentals by 10 cm^{-1}. This good agreement stems from the favorable error cancellation discussed in section 2.3. However, the numerical errors may severely affect the change of the dipole moment along the normal mode. Therefore, the IR intensity calculated according to ref 75 should be treated with caution.

Anharmonicities can be included via MD simulations. As expected, this effect is relatively small for CO stretching modes leading to a redshift of only 7 cm^{-1} compared to harmonic frequencies (cf. Figure 5). On the other hand, MD simulations represent an alternate way of calculating IR intensities.

4.2. Methanol Oxidation at Ceria (111)

The ODH of methanol at the thermodynamically most stable ceria surface of single-crystals,[165] thin-films,[158,160,161] and supported ceria nanoparticles exposing predominantly (111) facets [162] has been studied experimentally by TPD,[123,147,161] infrared reflection–adsorption spectroscopy (IRRAS),[158] non-contact atomic force microscopy (AFM),[159] and near-edge X-ray absorption fine structure spectroscopy (NEXAFS).[160]

These studies suggest that the formation of formaldehyde involves the following elementary steps: the dissociative adsorption of methanol discussed in the previous section and the

supposedly rate-determining H transfer from the methoxide to the surface, which results in formaldehyde and a second OH group. The entire catalytic cycle proceeds according to the Mars–van Krevelen mechanism,[32] which also involves water formation, desorption of formaldehyde and water (leading to a surface oxygen vacancy), and a fast re-oxidation step by molecular oxygen.

Compared with methanol at the pristine surface (**A1** in Figure 6), methanol adsorption at surface oxygen defects (**A2**) is significantly more exothermic. Pristine ceria surfaces are rather inactive in TPD experiments,[165] whereas partially reduced surfaces catalyze the oxidation of methanol to formaldehyde and CO_X. The selectivity towards CO_X increases with the degree of reduction.[166] However, mechanistic understanding of these observations is still missing.

To explain these observations, ref 2 discusses the oxidation of methanol at both surfaces. The mechanism for the initial oxidation step is shown in Figure 6. Along with the proton, an electron is transferred to the ceria surface. Thus, this step represents a proton-coupled electron transfer. The intrinsic barrier at the pristine surface (1.25 eV, dispersion-corrected PBE+U) is lower than at the defective surface (1.44 eV), which is plausible, as the reduced surface is expected to be a less effective oxidant. ZPVE lowers the intrinsic barrier by ca. 0.2 eV; dispersion corrections affect the barrier by less than 0.1 eV.

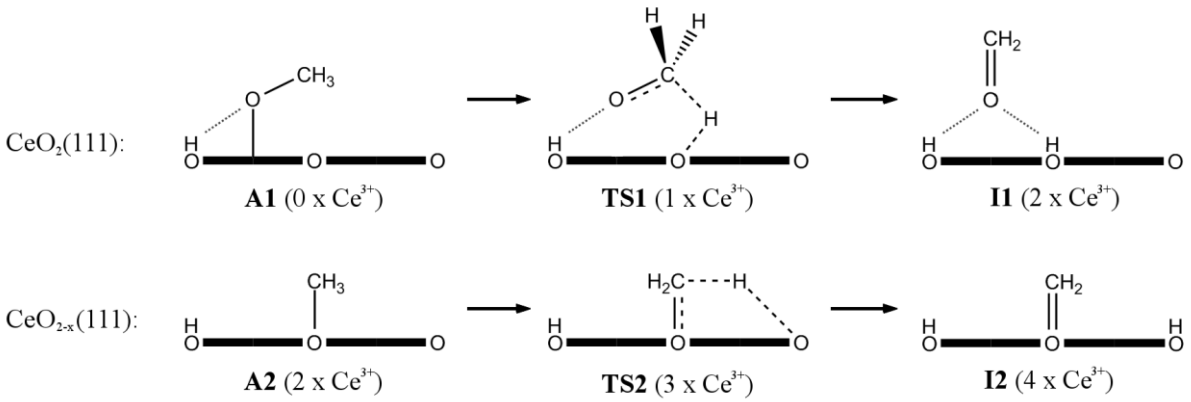

Figure 6: Reaction mechanism for the H transfer step at the pristine (above) and defective (below) ceria (111) surface. Dotted lines indicate H bonds, whereas dashed lines represent delocalized electrons. Reprinted with permission from ref 2. Copyright 2014 by the American Chemical Society.

Compared to HSE, PBE+U underestimates the oxygen defect formation energy for ceria surfaces (cf. Table 1), i.e., the reducibility is overestimated. Therefore, it is not surprising that PBE+U also underestimates the intrinsic barrier for the oxidation step compared to more accurate HSE. In fact, Truhlar and coworkers [167] have demonstrated that GGA functionals generally underestimate barrier heights compared to hybrid functionals.

Formaldehyde desorption competes with the formation of a bridging dioxymethylene species, which is assumed to be the key intermediate for deep oxidation.[160] Mechanisms for the oxidation of formaldehyde have been proposed in refs 168 and 169. As discussed in ref 4, the desorption energy is significantly smaller than the barrier for further oxidation. Thus, formaldehyde formation is preferred as observed in TPD experiments.[161]

At the beginning of a TPD experiment, the surface is pre-saturated with methanol. As the temperature increases, methanol desorption competes with the formation of formaldehyde. At the pristine surface, methanol desorption is favored, which is not reversible *in vacuo*. Due to the highly exothermic adsorption at surface vacancies, methanol oxidation is favored at these sites. The intrinsic barrier (1.44 eV, dispersion-corrected HSE in ref 2) is in good agreement with the experimental formaldehyde desorption barrier (1.5 eV, ref 123). Therefore, the higher methanol conversion at reduced ceria observed in ref 165 results from more exothermic methanol adsorption energies and does not indicate a higher catalytic activity.

4.3. Methanol Oxidation at Ceria (100)

In contrast to the ceria (111) surface, relatively few studies consider the (100) surface. Experimentally, methanol adsorption and dehydrogenation have been examined by Mullins and Albrecht;[161] Lopéz and coworkers [169] have studied the oxidation of methanol at ceria (100), (110), and (111) using DFT+U. As indicated by the lower oxygen defect formation energy at the (100) surface (cf. Table 1), this surface has the lower intrinsic barrier for the initial oxidation step. While the mechanism proposed in ref 169 predicts CO to be the sole oxidation product, ref 161 reports a mixture of formaldehyde and carbon oxides.

Ref 4 proposes a different mechanism for the deep oxidation and rationalizes the differences in activity and selectivity between ceria (100) and (111) with the three established concepts: coordinative unsaturation, degree of reduction, and reducibility (cf. ref 19).

The lower oxygen defect formation energies at the (100) surface are caused by the coordinative unsaturation making it the more reducible surface, i.e. the better oxidant. Likewise, methanol adsorbs very exothermically (-1.94 eV, dispersion-corrected PBE+U) at the (100) surface and reacts to formaldehyde with an intrinsic barrier of only 0.94 eV.[4] The resulting formaldehyde either desorbs or further reacts to a bridging methoxide species, which leads to deep oxidation as shown in Figure 7.

The desorption energy of formaldehyde amounts to 0.35 and 0.66 eV for the (111) and the (100) surface, respectively.[4] This pathway is furthermore favored by a gain in entropy. For the (111) surface, this amounts to $-T\Delta S$ = -0.56 eV at 300 K. The formation of the bridging dioxymethylene is highly exothermic at both surfaces, and the associated barrier is small. As a result, both pathways are competitive. For the (111) surface, the intrinsic barrier for the oxidation of formaldehyde amounts to ca. 1.7 eV,[168,169] thus formaldehyde desorption is favored over deep oxidation. At the (100) surface, this barrier is significantly smaller. Therefore, the formation of the bridging species becomes the decisive step for the selectivity of the methanol oxidation at ceria (100).[4]

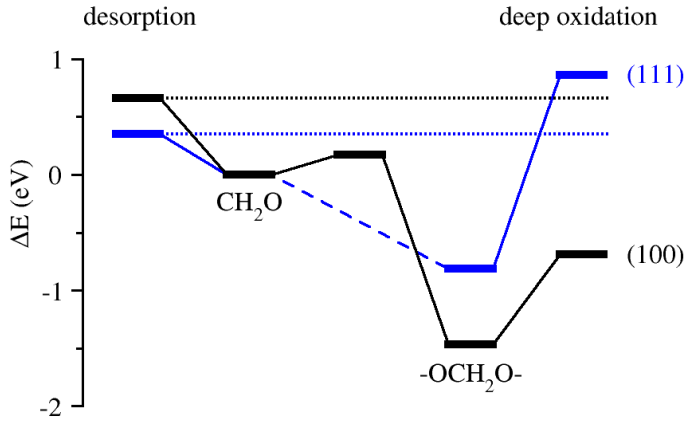

Figure 7: Reaction profiles for the formaldehyde desorption and oxidation at the ceria (111) and (100) surfaces (blue and black, respectively). Adapted with permission from ref 4. Copyright 2015 by the American Chemical Society.

These differences in reactivity are caused by the lower coordination numbers of Ce and O ions in the ceria (100) surface leading to more endothermic desorption energies and more exothermic dehydrogenation energies. A correlation between low coordination numbers and high activity has also been discussed by Vohs recently.[150]

A bidentate formate was found to be the most stable intermediate and as such, is expected to be the most abundant one. This is in good agreement with the IR experiments of Li *et al.*,[155] who observe formate formation starting at 473 K for polycrystalline ceria. No methanol could be detected after heating to 573 K.

Further oxidation leads to a negatively charged CO_2^- species that is bonded to the surface through both oxygen atoms–the charge is compensated by a Ce^{4+} counterion.[4] In contrast to molecular carbon dioxide, the anion is bent (132°) as this change in geometry lowers the $6a_1$ orbital ($2\pi^*$ in CO_2), which accommodates the 23rd electron. This is illustrated in the Walsh diagram in ref 170 (cf. Figure 1 of that reference).

Upon transferring an electron into the Ce *f* states, CO_2 can desorb, which is favored over CO desorption at low coverage.[4] However, this does not include temperature effects, which are known to affect the equilibrium between CO_2 and CO. Since the surface is oxidized upon CO desorption, the degree of surface reduction is also expected to affect the selectivity.

4.4. Methanol Oxidation at Vanadia-decorated Ceria (111)

At ceria-supported vanadia, the ODH of methanol occurs at much lower temperatures compared to pristine ceria and vanadia on inert supports; at low vanadia coverage, formaldehyde desorbs already at 370 K in TPD experiments.[123] The higher activity of ceria-supported catalysts compared to non-reducible supports such as alumina and silica has been rationalized using reactivity descriptors,[123,148] but detailed information on the support effect is still missing.

At the ceria-supported VO_2 monomer, methanol may adsorb by adding to the V=O group, by inserting into a V–O–Ce bond, or by adsorbing into the pseudovacancy in the ceria surface. As show in Table 3, adsorption energies obtained with dispersion-corrected HSE are similar for

Table 3. Methanol adsorption energies $E_0(ads)$ and intrinsic barriers $\Delta E_0^{\ddagger}$ for the initial oxidation step at different active sites obtained with dispersion-corrected density functionals. Values include ZPVE contributions. Pre-exponential factors (A) at T_{des} were obtained with eq. 3 using harmonic PBE+U frequencies.

	$E_0(ads)$ [eV]			$\Delta E_0^{\ddagger}$ [eV]			A [s^{-1}]	T_{des} [K]
	PBE+U	HSE	B3LYP	PBE+U	HSE	B3LYP		
CeO_{2-x} [a]	-2.39	-2.21		1.33	1.41		5.85×10^{11}	570
VO_2/CeO_2 [b]	-1.71	-1.86	-1.89	1.65	1.71	1.93	2.82×10^{12}	650
VO_2/CeO_2 [c]	-1.71	-1.86	-1.89	1.03	1.40	1.32	3.20×10^{12}	530
VO_2/CeO_2 [d]	-1.77	-1.86	-2.00	0.69	1.0 [f]		2.20×10^{13}	370
V_3O_6/CeO_2 [e]	-1.35	-1.65		1.30	1.4 [f]		6.06×10^{13}	500

[a] Ref 2; [b] ref 3 (methanol inserts into V–O–Ce bond, H transfer to V=O; Figure 8a); [c] ref 3 (methanol inserts into V–O–Ce bond, H transfer to surface O ion; Figure 8a); [d] ref 3 (methanol adsorbs into pseudovacancy, H transfer to vanadia O atom; Figure 8b); [e] ref 7; [f] Estimated by adding HSE corrections to the PBE+U value.

each adsorption site, though dispersion corrections stabilize the adsorption into the pseudovacancy more strongly, which is reasonable as the pseudovacancy represents a binding pocket. As a result, dispersion-corrected PBE+U and B3LYP predict a slightly more exothermic adsorption into the pseudovacancy because of the larger global scaling factors.[3] Methanol adsorption at the more stable vanadia trimer is less exothermic regardless of the functional.[7]

Methanol oxidation has been studied at the VO_2 monomer in ref 3. There is an error in some of the routines corresponding to the HSE hybrid functional in VASP 5.2.12 (Γ only), which was used in ref 3. The affected calculations have been repeated and corrected values are published in ref 7 along with adsorption and oxidation of methanol at the vanadia trimer. Adjustments are within 0.07 eV and do not change the conclusions qualitatively. The resulting reaction pathways are depicted in Figure 8.

Starting with a vanadium-bonded methoxide, hydrogen may be transferred to the V=O group or to a surface oxygen ion (cf. Figure 8a). The hydrogen transfer to the vanadyl oxygen atom ($\Delta E^{\ddagger}$ = 1.93 eV, B3LYP) is accompanied by an electron transfer into the V *d* states. For vanadia supported on non-reducible silica, a similar oxidation pathway has been calculated with an intrinsic barrier of 1.97 eV (B3LYP).[35] The authors report that B3LYP overestimates the barrier

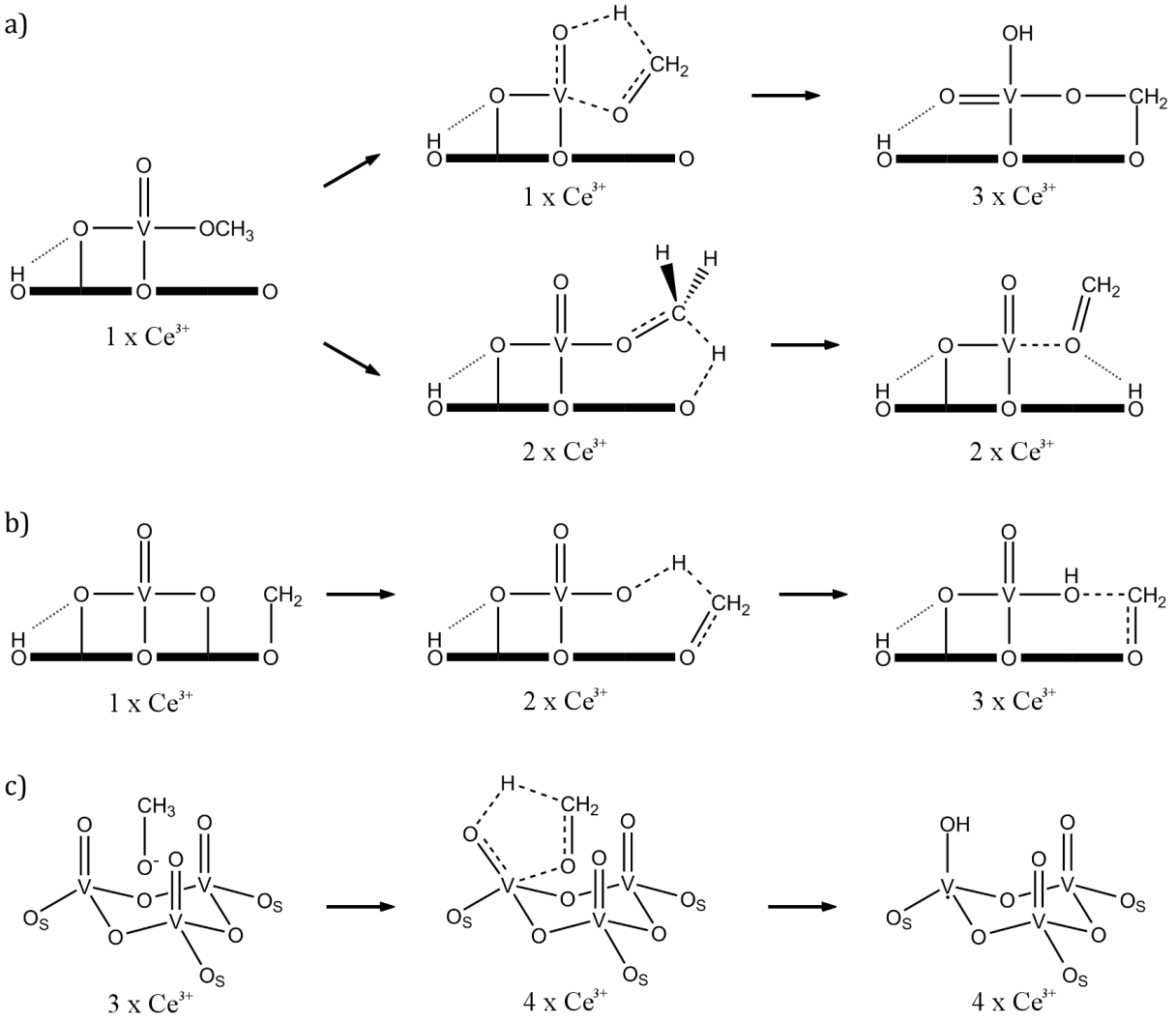

Figure 8. Reaction mechanisms for the hydrogen transfer step from various methanol adsorption structures at vanadia-decorated ceria (111). Dotted lines represent hydrogen bonds, whereas dashed lines represent delocalized electrons. O_S represents surface O ions. Adapted with permission from ref 3. Copyright 2014 by the American Chemical Society.

by 0.17 eV compared to a CCSD(T) reference. As shown in Table 3, B3LYP also predicts a higher barrier compared to PBE+U and HSE. Based on the results of ref 35, the barrier obtained with HSE is considered more reliable. However, hydrogen transfer to the surface oxygen ion is favored regardless of the functional, because the electron is transferred into the energetically lower Ce *f* states.[3] This represents the electronic support effect of ceria.

Upon adsorption into the pseudovacancy, hydrogen can be transferred to an interphase oxygen atom (cf. Figure 8b). Here, the methoxide is oriented into a productive arrangement with a short O ↔ H distance (220 pm compared to more than 300 pm for other adsorption structures)

facilitating the hydrogen transfer. As a result, the entropy of activation is lowered leading to a higher pre-exponential factor *A* (cf. Table 3). Such structural effects are well-known in enzyme catalysis (e.g., ref 171). In addition, electrons are transferred into the Ce *f* states leading to a highly complex support effect that goes far beyond a mere electronic polarization.

At the vanadia trimer (cf. Figure 8c), hydrogen can only be transferred to vanadyl oxygen atoms, which involves partially occupied V *d* states.[7] As a result, the intrinsic barrier is higher than the one obtained for the VO_2 monomer. However, three symmetrically equivalent vanadyl groups are available, which increases the rate by a factor of 3. This is already included in the pre-exponential factor in Table 3.

According to the reaction mechanism discussed in ref 3, the intrinsic barrier for the hydrogen transfer step is also the barrier for formaldehyde desorption. For a more detailed comparison with the experiments by Freund and coworkers,[123,147] TPD spectra have been simulated by integrating the Eyring–Polanyi equation derived in section 1.2 with a constant heating rate of 3 K/s, which was also used in the experiment. At temperatures above 300 K, quantum effects calculated using eq. 4 were found to be small and are therefore neglected.

Intrinsic barriers and the corresponding formaldehyde desorption temperatures are compiled in Table 3. The desorption rates (normalized to $\theta_0 = 1$) are plotted in Figure 9 along with the experimental TPD spectra recorded for low vanadia coverage before and after sintering as published in refs 123 and 147.

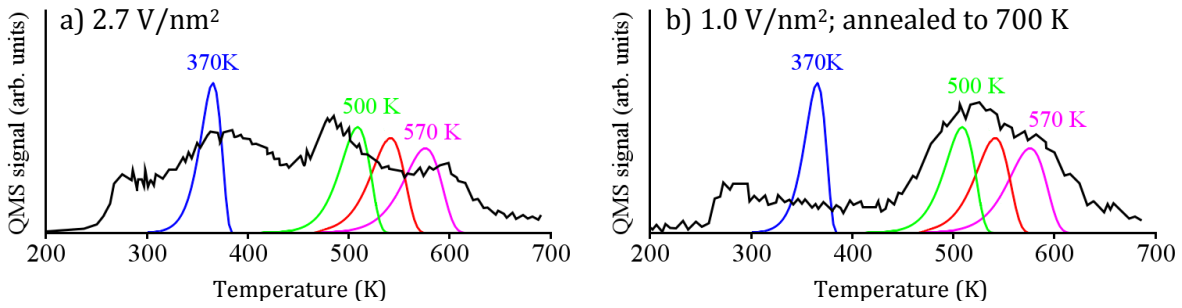

Figure 9. Experimental TPD spectra [123,147] (black lines) along with the simulated formaldehyde desorption peaks at VO_2/CeO_2 (blue and red), V_3O_6/CeO_2 (green), and CeO_2 (purple). Adapted with permission from ref 3. Copyright 2014 by the American Chemical Society.

The α desorption peak at 370 K is assigned to the kinetically favored oxidation pathway following methanol adsorption into the pseudovacancy next to the VO_2 monomer. This peak is only observed at low vanadia coverage,[123] which is in good agreement with this assignment. As discussed in section 4.2, the γ desorption peak at 570 K is assigned to the methanol oxidation at the ceria (111) surface. The β desorption peak at ca. 500 K can be either assigned to the reaction at the trimer or at the monomer.

This assignment is somewhat surprising given that the intrinsic barrier for the methanol oxidation at the VO_2 trimer is actually higher than the barrier for the vanadia-free surface (cf. Table 3). However, pre-exponential factors differ by two orders of magnitude leading to a lower desorption temperature for the trimer. This illustrates the importance of evaluating both enthalpy and entropy of activation.

Experimental barriers are typically derived via Redhead analysis,[172] i.e. the TPD spectrum is fitted with eq. 3 assuming a pre-exponential factor of 10^{13} s^{-1}, which is close to the values reported in Table 3. Thus, caution is advised when comparing experimental and theoretical barriers. Furthermore, the kinetic model presented in ref 3 is unable to account for equilibria between different adsorption structures. This is expected to significantly broaden the peaks.

4.5. Water Adsorption at Ceria Surfaces

Experimentally, water adsorption at ceria surfaces has been studied using XPS,[173-176] TPD,[173-177] and scanning force microscopy (SFM).[178] Peden and coworkers[174] report water desorption at 265 K for ceria (111) films at low water coverage. At high coverage, water desorbs already at 195 K with a shoulder at 265 K in the TPD spectrum. This shoulder is more pronounced for partially reduced ceria films. Mullins et al.[175] report three broad but distinct desorption peaks for ceria (100) at 200 K, 300 K, and 400 K. These higher desorption temperatures are accompanied by a larger amount of dissociative adsorption as indicated by XPS spectra.[175]

The adsorption of water monomers at the ceria (111) surface has been studied using different DFT approaches (cf. refs 179-184). These studies report multiple molecular adsorption structures that vary in the tilting angle of the water molecule toward the surface. Water

dissociation leads to a hydroxyl pair with a H bond between the H^+ and the OH^- moiety, i.e. a dynamic ion pair (cf. ref 185). Molecular and dissociative adsorption energies are similar for medium-sized unit cells, i.e. $p(2\times2)$ or $p(3\times3)$,[182-184] but at the small $p(1\times1)$ cell, molecular adsorption is significantly favored.[184] This is due to surface strain induced by pronounced relaxation of oxygen ions upon protonation. So far, theory cannot explain the two water desorption peaks at the ceria (111) surface (e.g., ref 174), which is due to an incomplete exploration of the potential energy surface of water on ceria surfaces as suggested in ref 18.

To assign the TPD peaks, ref 6 discusses monomeric and oligomeric water adsorption structures at ceria (111). At low coverage, water forms particularly stable dimers that cause the desorption peak at 265 K. Similar structures have also been reported at the $Fe_3O_4(111)$ and the $ZnO(10\bar{1}0)$ surface (cf. refs 186 and 187, respectively).

Water adsorption at surface OH groups is comparably exothermic. Such OH groups are formed when water adsorbs into oxygen vacancies. This explains why reduced ceria films bind water more strongly, which has been observed in ref 174.

At high coverage, an amorphous monolayer is formed at the (111) surface (cf. Figure 10). In agreement with XPS results,[175] water adsorbs predominantly molecularly. Such molecular adsorption structures are assigned to the water desorption peak at 195 K.[174,175]

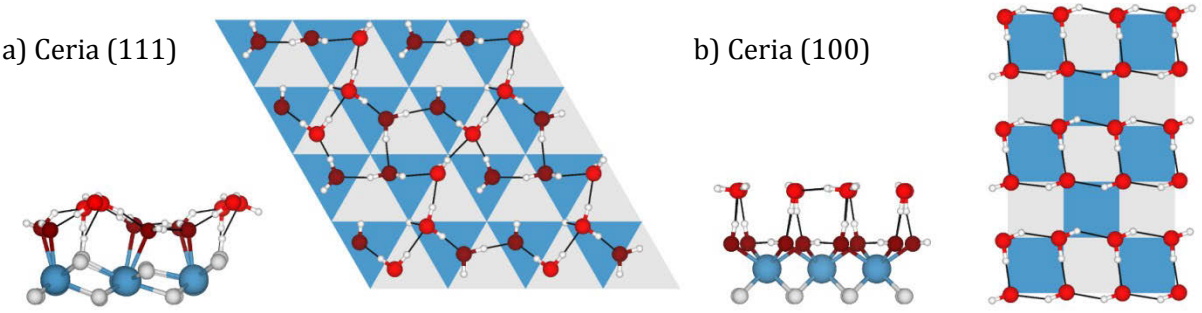

Figure 10. Side and top views on water monolayers at the pristine ceria (111) and (100) surfaces. For the (111) surface (a), O atoms of water molecules (on top of Ce ions) are (dark) red. For the (100) surface (b), surface OH groups are dark red, and water O atoms are red. For the top views, Ce ions are represented by blue polygons; each vertex represents a surface O ion.

Parker and coworkers[184] also report monomeric adsorption structures for the ceria (110) and (100) surfaces: in both cases, dissociative adsorption is favored even at high water coverage, and adsorption energies increase following (111) < (110) < (100),[184] which coincides with an increase in the surface energies.

At the (100) surface, water adsorbs dissociatively until the entire surface is hydroxylated.[6] This corresponds to a water coverage of 1 H_2O per surface Ce ion. Via a template effect, this hydroxylated surface enables a well-ordered "square ice" monolayer. Similar monolayers have been recently observed in graphene nanocapillaries.[188] Due to the formation of this highly stable monolayer, ceria (100) becomes the more stable surface termination in the presence of water.[6] This passivation will also decrease the catalytic activity of ceria (100) facets.

4.6. Hydrogen Evolution at Ceria Surfaces

Two surface OH groups may recombine forming either water (eq. 21) or molecular hydrogen (eq. 22). While water desorption does not change the degree of surface reduction, i.e. the number of Ce^{3+} ions, H_2 evolution oxidizes the surface.

$$[2Ce^{3+}, 2O^{2-}, 2OH^{-}] \rightarrow [2Ce^{3+}, 3O^{2-}, V_O] + H_2O \quad (21)$$

$$[2Ce^{3+}, 2O^{2-}, 2OH^{-}] \rightarrow [2Ce^{4+}, 4O^{2-}] + H_2 \quad (22)$$

For ceria (111), PBE+U predicts similar free desorption energies for both pathways, whereas H_2 evolution is favored when using the HSE hybrid functional.[2] The desorption enthalpies compiled in Table 4 predict the same selectivity, though barriers would be required for a definite answer.

Table 4: Desorption enthalpies (ΔH) and entropies (ΔS; 300 K and 0.1 MPa) in eV for water and hydrogen obtained with dispersion-corrected PBE+U and HSE at different ceria surfaces.

	H_2 evolution			Water desorption		
	ΔH_{PBE+U}	ΔH_{HSE}	$-T\Delta S_{PBE+U}$	ΔH_{PBE+U}	ΔH_{HSE}	$-T\Delta S_{PBE+U}$
$CeO_2(111)$ [a]	2.30	1.81	-0.55	2.12	2.04	-0.53
$CeO_2(100)$ [b]	3.19			2.27		

[a] Ref 2; [b] ref 4.

For the hydrogen evolution, two desorption pathways have been studied using PBE+U.[189-191] The intrinsic barrier for the direct recombination is higher than the barrier for the formation of a H^- ion coordinated to a Ce^{4+} ion, which then reacts with an OH group to form H_2.[190,191] However, the desorption barriers are expected to depend strongly on the chosen density functional as indicated by the large discrepancies between the reaction energies obtained with HSE and PBE+U (cf. Table 4). Barriers for the water desorption are not available.

Experimentally, hydrogen evolution is observed.[161] Based on reaction energies, PBE+U fails to predict the correct desorption product as oxygen vacancy formation energies are significantly underestimated, i.e. the surface reducibility is overestimated (cf. Table 1).

At the ceria (100) surface, water desorption is strongly favored over H_2 evolution when using PBE+U (cf. Table 4). For this surface, the difference between the oxygen defect formation energies obtained with PBE+U and HSE (cf. Table 1) is only 0.28 eV. Thus, it is inferred that water desorption occurs regardless of the functional used. These calculations refer to the low coverage limit for the oxidized (100) surface. Albrecht and Mullins [161] observed both water and H_2 for oxidized ceria (100) films, whereas reduced ceria films yield exclusively H_2. Thus, the selectivity depends strongly on the degree of surface reduction.

As a result, the ODH of methanol may actually follow eq. 23 (cf. methanol reforming) instead of the mechanism stated in section 1.2 depending on the reducibility of the catalyst. This alternative mechanism does not include a reoxidation step.

$$CH_3OH \rightarrow CH_2O + H_2 \qquad (23)$$

5. Conclusions

Ceria catalysts can activate C–H bonds as demonstrated using the ODH of methanol as a model reaction under idealized conditions (low pressure, well-ordered surfaces). Among other factors, activity and selectivity depend on the surface orientation. Methanol adsorption structures at different active sites can be distinguished by their CO stretching band. Thus, it should be possible to quantify active sites using methanol as an IR probe. The lower defect formation energies at the pristine (100) surface are caused by the coordinative unsaturation making it the more reducible surface, i.e. the better oxidant. In addition, formaldehyde binds more strongly to the (100) surface, and is therefore more likely oxidized to carbon oxides lowering the selectivity of the methanol oxidation at ceria (100) compared to ceria (111).

The activity can also be increased by depositing small vanadia clusters on ceria surfaces. This leads to an oxygen spillover from ceria to the vanadia cluster resulting in a pseudovacancy in the surface, which represents a highly exothermic adsorption site. The methoxide is then oxidized via a proton-coupled electron transfer: while the proton is transferred to the vanadia cluster, the electron is transferred into the Ce *f* states. A similar support effect has been predicted for anatase-supported vanadia.[192] Upon methanol adsorption at the V–O–Ti interphase bond, the proton is transferred to a surface oxygen ion, and both electrons are transferred into Ti *d* states. At non-reducible supports such as silica, the vanadia cluster is reduced instead, which is accompanied by a higher barrier.

Small vanadia clusters supported on ceria (111) also provide a special binding site for the substrate, i.e. the pseudovacancy, which enables an oxidation pathway with a particularly low barrier. As a result, the activity of the supported vanadia clusters decreases with their nuclearity as predicted by reactivity descriptors. Thus, to fully utilize the support effect between both oxides, a support is needed that stabilizes small vanadia clusters even at high temperatures. At the ceria (111) surface, vanadia monomers agglomerate at the temperatures needed to convert methanol to formaldehyde.

For methanol at ceria surfaces, harmonic wavenumbers for the C–O stretching modes obtained with the gradient-corrected density functional PBE+U are in good agreement with experimental fundamentals, and adsorption energies are similar for each density functional employed in this work. Desorption temperatures obtained using HSE barriers are in good agreement with experimentally observed values, but intrinsic barriers obtained with PBE+U are underestimated by up to 0.4 eV compared to the more accurate hybrid functionals. This is a known shortcoming of GGA functionals.[167]

While the pristine ceria (111) surface has a lower surface energy than the polar (100) surface, the hydrated (100) surface is the most stable surface for higher chemical potentials of water. This is due to the formation of a well-ordered water monolayer on the fully hydroxylated (100) surface, which compensates the surface dipole. The ceria (111) surface binds water less strongly and favors molecular adsorption. Thus, the chemical potential of water affects the relative stability of ceria (111) and (100), which is relevant for the synthesis of ceria particles in aqueous solution. This case study illustrates the impact of coordinative unsaturation, morphology, and electrostatics on the water–surface interactions.

The results discussed in this work refer to idealized solid–gas interfaces. These highly simplified model systems are not expected to reproduce the properties of real working catalysts. Instead, they capture the essential features of the system, and by combining experimental and theoretical model studies, atomistic understanding may be obtained. Thus, relationships between structure, composition, catalytic activity, and selectivity may be identified, which will help to tailor ceria-based catalysts to the specific requirements for industrial application.

6. BIBLIOGRAPHY

(1) Paier, J.; **Kropp, T.**; Penschke, C.; Sauer, J. Stability and Migration Barriers of Small Vanadium Oxide Clusters on the CeO_2(111) Surface Studied by Density Functional Theory. *Faraday Discuss.* **2013**, *162*, 233-245.

(2) **Kropp, T.**; Paier, J. Reactions of Methanol with Pristine and Defective Ceria (111) Surfaces: A Comparison of Density Functionals. *J. Phys. Chem. C* **2014**, *118*, 23690.

(3) **Kropp, T.**; Paier, J.; Sauer, J. Support Effect in Oxide Catalysis: Methanol Oxidation on Vanadia/Ceria. *J. Am. Chem. Soc.* **2014**, *136*, 14616-14625.

(4) **Kropp, T.**; Paier, J. Activity Versus Selectivity of the Methanol Oxidation at Ceria Surfaces: A Comparative First-Principles Study. *J. Phys. Chem. C* **2015**, *119*, 23021-23031.

(5) Yang, C.; Bebensee, F.; Nefedov, A.; Wöll, C.; **Kropp, T.**; Komissarov, L.; Penschke, C.; Moerer, R.; Paier, J.; Sauer, J. Methanol Adsorption on Monocrystalline Ceria Surfaces. *J. Catal.* **2016**, 336, 116-125.

(6) **Kropp, T.**; Paier, J.; Sauer, J. Interactions of Water with the (111) and (100) Surfaces of Ceria. *Phys. Chem. Chem. Phys.* **2016**, in preparation.

(7) **Kropp, T.**; Paier, J.; Sauer, J. Selective Methanol Oxidation at Ceria-Supported Vanadia Oligomers. *J. Phys. Chem. C* **2016**, in preparation.

(8) Thomas, J. M.; Thomas, W. J. *Principles and Practice of Heterogeneous Catalysis*; Wiley, **1997**.

(9) Somorjai, G. A.; Li, Y. *Introduction to Surface Chemistry and Catalysis*; John Wiley & Sons, **2010**.

(10) Sauer, J.; Freund, H.-J. Models in Catalysis. *Catal. Lett.* **2015**, *145*, 109-125.

(11) Ertl, G. Reactions at Surfaces: From Atoms to Complexity (Nobel Lecture). *Angew. Chem. Int. Ed.* **2008**, *47*, 3524-3535.

(12) Böhme, D. K.; Schwarz, H. Gas-Phase Catalysis by Atomic and Cluster Metal Ions: The Ultimate Single-Site Catalysts. *Angew. Chem. Int. Ed.* **2005**, *44*, 2336-2354.

(13) Ertl, G.; Knözinger, H.; Weitkamp, J. Characterization of Solid Catalysts. In *Handbook of Heterogeneous Catalysis*; Wiley-VCH Verlag GmbH & Co. KGaA, **2008**.

(14) Kohn, W.; Sham, L. J. Self-Consistent Equations Including Exchange and Correlation Effects. *Phys. Rev.* **1965**, *140*, 1133.

(15) Jones, R. O.; Gunnarsson, O. The Density Functional Formalism, Its Applications and Prospects. *Rev. Mod. Phys.* **1989**, *61*, 689-746.

(16) Werner, H.-J.; Schütz, M. An Efficient Local Coupled Cluster Method for Accurate Thermochemistry of Large Systems. *J. Chem. Phys.* **2011**, *135*, 144116.

(17) Huang, P.; Carter, E. A. Advances in Correlated Electronic Structure Methods for Solids, Surfaces, and Nanostructures. *Annu. Rev. Phys. Chem.* **2008**, *59*, 261-290.

(18) Paier, J.; Penschke, C.; Sauer, J. Oxygen Defects and Surface Chemistry of Ceria: Quantum Chemical Studies Compared to Experiment. *Chem. Rev.* **2013**, *113*, 3949-3985.

(19) Barteau, M. A. Organic Reactions at Well-Defined Oxide Surfaces. *Chem. Rev.* **1996**, *96*, 1413-1430.

(20) Ertl, G.; Knözinger, H.; Weitkamp, J. General Principles, Methods, and Reaction Engineering. In *Handbook of Heterogeneous Catalysis*; Wiley-VCH Verlag GmbH & Co. KGaA, **2008**.

(21) Langmuir, I. Chemical Reactions at Low Pressures. *J. Am. Chem. Soc.* **1915**, *37*, 1139-1167.

(22) Zecchina, A.; Arean, C. O. Diatomic Molecular Probes for Mid-IR Studies of Zeolites. *Chem. Soc. Rev.* **1996**, *25*, 187-197.

(23) Tatibouët, J. M. Methanol Oxidation as a Catalytic Surface Probe. *Appl. Catal. A* **1997**, *148*, 213-252.

(24) Brunauer, S.; Emmett, P. H.; Teller, E. Adsorption of Gases in Multimolecular Layers. *J. Am. Chem. Soc.* **1938**, *60*, 309-319.

(25) Atkins, P.; de Paula, J. *Atkins' Physical Chemistry*; OUP Oxford, **2010**.

(26) Eyring, H. The Transmission Coefficient in Reaction Rate Theory. *Rev. Mod. Phys.* **1962**, *34*, 616-619.

(27) Wigner, E. Concerning the Excess of Potential Barriers in Chemical Reactions. *Z. Phys. Chem. B* **1932**, *19*, 203-216.

(28) Fermann, J. T.; Auerbach, S. Modeling Proton Mobility in Acidic Zeolite Clusters: II. Room Temperature Tunneling Effects from Semiclassical Rate Theory. *J. Chem. Phys.* **2000**, *112*, 6787-6794.

(29) Marcus, R. A.; Sutin, N. Electron Transfers in Chemistry and Biology. *BBA - Bioenergetics* **1985**, *811*, 265-322.

(30) Chaichian, M.; Demichev, A. *Path Integrals in Physics: Volume I Stochastic Processes and Quantum Mechanics*; Taylor & Francis, **2001**.

(31) Nørskov, J. K.; Abild-Pedersen, F.; Studt, F.; Bligaard, T. Density Functional Theory in Surface Chemistry and Catalysis. *Proc. Natl. Acad. Sci. U.S.A.* **2011**, *108*, 937-943.

(32) Mars, P.; van Krevelen, D. W. Oxidations Carried out by Means of Vanadium Oxide Catalysts. *Chem. Eng. Sci.* **1954**, *3, Supplement 1*, 41-59.

(33) Sauer, J.; Döbler, J. Structure and Reactivity of V_2O_5: Bulk Solid, Nanosized Clusters, Species Supported on Silica and Alumina, Cluster Cations and Anions. *Dalton Trans.* **2004**, *19*, 3116-3121.

(34) Kim, H. Y.; Lee, H. M.; Pala, R. G. S.; Metiu, H. Oxidative Dehydrogenation of Methanol to Formaldehyde by Isolated Vanadium, Molybdenum, and Chromium Oxide Clusters Supported on Rutile TiO_2(110). *J. Phys. Chem. C* **2009**, *113*, 16083-16093.

(35) Döbler, J.; Pritzsche, M.; Sauer, J. Oxidation of Methanol to Formaldehyde on Supported Vanadium Oxide Catalysts Compared to Gas Phase Molecules. *J. Am. Chem. Soc.* **2005**, *127*, 10861-10868.

(36) Bronkema, J. L.; Bell, A. T. Mechanistic Studies of Methanol Oxidation to Formaldehyde on Isolated Vanadate Sites Supported on MCM-48. *J. Phys. Chem. C* **2007**, *111*, 420-430.

(37) Dirac, P. A. M. Quantum Mechanics of Many-Electron Systems. *Proc. R. Soc. A* **1929**, *123*, 714-733.

(38) Born, M.; Oppenheimer, R. Zur Quantentheorie Der Molekeln. *Ann. Phys.* **1927**, *389*, 457-484.

(39) Roothaan, C. C. J. New Developments in Molecular Orbital Theory. *Rev. Mod. Phys.* **1951**, *23*, 69-89.

(40) Hohenberg, P.; Kohn, W. Inhomogeneous Electron Gas. *Phys. Rev. B* **1964**, *136*, B864.

(41) Perdew, J. P. *Electronic Structure of Solids' 91*; Akademie Verlag, Berlin, **1991**.

(42) Perdew, J. P.; Burke, K.; Ernzerhof, M. Generalized Gradient Approximation Made Simple. *Phys. Rev. Lett.* **1996**, *77*, 3865-3868.

(43) Becke, A. D. Density-Functional Exchange-Energy Approximation with Correct Asymptotic Behavior. *Phys. Rev. A* **1988**, *38*, 3098-3100.

(44) Lee, C.; Yang, W.; Parr, R. G. Development of the Colle-Salvetti Correlation-Energy Formula into a Functional of the Electron Density. *Phys. Rev. B* **1988**, *37*, 785-789.

(45) Perdew, J. P.; Ernzerhof, M.; Burke, K. Rationale for Mixing Exact Exchange with Density Functional Approximations. *J. Chem. Phys.* **1996**, *105*, 9982-9985.

(46) Heyd, J.; Scuseria, G. E.; Ernzerhof, M. Hybrid Functionals Based on a Screened Coulomb Potential. *J. Chem. Phys.* **2003**, *118*, 8207-8215.

(47) Krukau, A. V.; Vydrov, O. A.; Izmaylov, A. F.; Scuseria, G. E. Influence of the Exchange Screening Parameter on the Performance of Screened Hybrid Functionals. *J. Chem. Phys.* **2006**, *125*, 224106.

(48) Becke, A. D. Density-Functional Thermochemistry 3. The Role of Exact Exchange. *J. Chem. Phys.* **1993**, *98*, 5648-5652.

(49) Vosko, S. H.; Wilk, L.; Nusair, M. Accurate Spin-Dependent Electron Liquid Correlation Energies for Local Spin Density Calculations: A Critical Analysis. *Can. J. Phys.* **1980**, *58*, 1200-1211.

(50) Anisimov, V. I.; Zaanen, J.; Andersen, O. K. Band Theory and Mott Insulators - Hubbard-U Instead of Stoner-I. *Phys. Rev. B* **1991**, *44*, 943-954.

(51) Liechtenstein, A. I.; Anisimov, V. I.; Zaanen, J. Density-Functional Theory and Strong-Interactions - Orbital Ordering in Mott-Hubbard Insulators. *Phys. Rev. B* **1995**, *52*, R5467-R5470.

(52) Kohn, W.; Meir, Y.; Makarov, D. E. Van Der Waals Energies in Density Functional Theory. *Phys. Rev. Lett.* **1998**, *80*, 4153-4156.

(53) Tkatchenko, A.; Scheffler, M. Accurate Molecular Van Der Waals Interactions from Ground-State Electron Density and Free-Atom Reference Data. *Phys. Rev. Lett.* **2009**, *102*, 073005.

(54) Grimme, S.; Antony, J.; Ehrlich, S.; Krieg, H. A Consistent and Accurate Ab Initio Parametrization of Density Functional Dispersion Correction (DFT-D) for the 94 Elements H-Pu. *J. Chem. Phys.* **2010**, *132*, 154104.

(55) Zhao, Y.; Truhlar, D. G. Applications and Validations of the Minnesota Density Functionals. *Chem. Phys. Lett.* **2011**, *502*, 1-13.

(56) Dion, M.; Rydberg, H.; Schröder, E.; Langreth, D. C.; Lundqvist, B. I. Van Der Waals Density Functional for General Geometries. *Phys. Rev. Lett.* **2004**, *92*, 246401.

(57) Kannemann, F. O.; Becke, A. D. Van Der Waals Interactions in Density-Functional Theory: Rare-Gas Diatomics. *J. Chem. Theory Comput.* **2009**, *5*, 719-727.

(58) Grimme, S. Semiempirical Gga-Type Density Functional Constructed with a Long-Range Dispersion Correction. *J. Comput. Chem.* **2006**, *27*, 1787-1799.

(59) Bloch, F. Über Die Quantenmechanik Der Elektronen in Kristallgittern. *Z. Physik* **1929**, *52*, 555-600.

(60) Phillips, J. C.; Kleinman, L. New Method for Calculating Wave Functions in Crystals and Molecules. *Phys. Rev.* **1959**, *116*, 287-294.

(61) von Barth, U.; Gelatt, C. D. Validity of the Frozen-Core Approximation and Pseudopotential Theory for Cohesive Energy Calculations. *Phys. Rev. B* **1980**, *21*, 2222-2228.

(62) Hamann, D. R.; Schlüter, M.; Chiang, C. Norm-Conserving Pseudopotentials. *Phys. Rev. Lett.* **1979**, *43*, 1494-1497.

(63) Kerker, G. P. Non-Singular Atomic Pseudopotentials for Solid State Applications. *J. Phys. C: Solid State Phys.* **1980**, *13*, L189.

(64) Bachelet, G. B.; Hamann, D. R.; Schlüter, M. Pseudopotentials That Work: From H to Pu. *Phys. Rev. B* **1982**, *26*, 4199-4228.

(65) Troullier, N.; Martins, J. L. Efficient Pseudopotentials for Plane-Wave Calculations. *Phys. Rev. B* **1991**, *43*, 1993-2006.

(66) Blöchl, P. E. Projector Augmented-Wave Method. *Phys. Rev. B* **1994**, *50*, 17953-17979.

(67) Kresse, G.; Joubert, D. From Ultrasoft Pseudopotentials to the Projector Augmented-Wave Method. *Phys. Rev. B* **1999**, *59*, 1758-1775.

(68) Baldereschi, A. Mean-Value Point in the Brillouin Zone. *Phys. Rev. B* **1973**, *7*, 5212-5215.

(69) Chadi, D. J.; Cohen, M. L. Special Points in the Brillouin Zone. *Phys. Rev. B* **1973**, *8*, 5747-5753.

(70) Monkhorst, H. J.; Pack, J. D. Special Points for Brillouin-Zone Integrations. *Phys. Rev. B* **1976**, *13*, 5188-5192.

(71) MacDonald, A. H. Comment on Special Points for Brillouin-Zone Integrations. *Phys. Rev. B* **1978**, *18*, 5897-5899.

(72) Moreno, J.; Soler, J. M. Optimal Meshes for Integrals in Real- and Reciprocal-Space Unit Cells. *Phys. Rev. B* **1992**, *45*, 13891-13898.

(73) Campbell, C. T.; Sellers, J. R. V. The Entropies of Adsorbed Molecules. *J. Am. Chem. Soc.* **2012**, *134*, 18109-18115.

(74) Alecu, I. M.; Zheng, J. J.; Zhao, Y.; Truhlar, D. G. Computational Thermochemistry: Scale Factor Databases and Scale Factors for Vibrational Frequencies Obtained from Electronic Model Chemistries. *J. Chem. Theory Comput.* **2010**, *6*, 2872-2887.

(75) Porezag, D.; Pederson, M. R. Infrared Intensities and Raman-Scattering Activities within Density-Functional Theory. *Phys. Rev. B* **1996**, *54*, 7830-7836.

(76) Borysow, J.; Moraldi, M.; Frommhold, L. The Collision Induced Spectroscopies. *Mol. Phys.* **1985**, *56*, 913-922.

(77) Gaigeot, M.-P.; Sprik, M. Ab Initio Molecular Dynamics Computation of the Infrared Spectrum of Aqueous Uracil. *J. Phys. Chem. B* **2003**, *107*, 10344-10358.

(78) Torrie, G. M.; Valleau, J. P. Nonphysical Sampling Distributions in Monte Carlo Free-Energy Estimation: Umbrella Sampling. *J. Comput. Phys.* **1977**, *23*, 187-199.

(79) Straatsma, T. P.; Berendsen, H. J. C. Free Energy of Ionic Hydration: Analysis of a Thermodynamic Integration Technique to Evaluate Free Energy Differences by Molecular Dynamics Simulations. *J. Chem. Phys.* **1988**, *89*, 5876-5886.

(80) Claeyssens, F.; Harvey, J. N.; Manby, F. R.; Mata, R. A.; Mulholland, A. J.; Ranaghan, K. E.; Schütz, M.; Thiel, S.; Thiel, W.; Werner, H.-J. High-Accuracy Computation of Reaction Barriers in Enzymes. *Angew. Chem. Int. Ed.* **2006**, *45*, 6856-6859.

(81) Fukui, K. Formulation of the Reaction Coordinate. *J. Phys. Chem.* **1970**, *74*, 4161-4163.

(82) Cerjan, C. J.; Miller, W. H. On Finding Transition States. *J. Chem. Phys.* **1981**, *75*, 2800-2806.

(83) Baker, J. An Algorithm for the Location of Transition States. *J. Comput. Chem.* **1986**, *7*, 385-395.

(84) Henkelman, G.; Jonsson, H. A Dimer Method for Finding Saddle Points on High Dimensional Potential Surfaces Using Only First Derivatives. *J. Chem. Phys.* **1999**, *111*, 7010-7022.

(85) Heyden, A.; Bell, A. T.; Keil, F. J. Efficient Methods for Finding Transition States in Chemical Reactions: Comparison of Improved Dimer Method and Partitioned Rational Function Optimization Method. *J. Chem. Phys.* **2005**, *123*, 224101.

(86) Malek, R.; Mousseau, N. Dynamics of Lennard-Jones Clusters: A Characterization of the Activation-Relaxation Technique. *Phys. Rev. E* **2000**, *62*, 7723-7728.

(87) Halgren, T. A.; Lipscomb, W. N. The Synchronous-Transit Method for Determining Reaction Pathways and Locating Molecular Transition States. *Chem. Phys. Lett.* **1977**, *49*, 225-232.

(88) Peng, C.; Bernhard Schlegel, H. Combining Synchronous Transit and Quasi-Newton Methods to Find Transition States. *Isr. J. Chem.* **1993**, *33*, 449-454.

(89) Peng, C.; Ayala, P. Y.; Schlegel, H. B.; Frisch, M. J. Using Redundant Internal Coordinates to Optimize Equilibrium Geometries and Transition States. *J. Comput. Chem.* **1996**, *17*, 49-56.

(90) Mills, G.; Jonsson, H.; Schenter, G. K. Reversible Work Transition-State Theory - Application to Dissociative Adsorption of Hydrogen. *Surf. Sci.* **1995**, *324*, 305-337.

(91) H. Jonsson; G. Mills; Jacobsen, K. W. Nudged Elastic Band Method for Finding Minimum Energy Paths of Transitions. In *Classical and Quantum Dynamics in Condensed Phase Simulations*; J. Berne, G. Ciccotti, Coker, D. F., Eds.; World Scientific, **1998**.

(92) Henkelman, G.; Uberuaga, B. P.; Jonsson, H. A Climbing Image Nudged Elastic Band Method for Finding Saddle Points and Minimum Energy Paths. *J. Chem. Phys.* **2000**, *113*, 9901-9904.

(93) E, W.; Ren, W.; Vanden-Eijnden, E. String Method for the Study of Rare Events. *Phys. Rev. B* **2002**, *66*, 052301.

(94) E, W.; Ren, W.; Vanden-Eijnden, E. Simplified and Improved String Method for Computing the Minimum Energy Paths in Barrier-Crossing Events. *J. Chem. Phys.* **2007**, *126*, 164103.

(95) Peters, B.; Heyden, A.; Bell, A. T.; Chakraborty, A. A Growing String Method for Determining Transition States: Comparison to the Nudged Elastic Band and String Methods. *J. Chem. Phys.* **2004**, *120*, 7877-7886.

(96) Laio, A.; Parrinello, M. Escaping Free-Energy Minima. *Proc. Natl. Acad. Sci. U.S.A.* **2002**, *99*, 12562-12566.

(97) Maeda, S.; Morokuma, K. Finding Reaction Pathways of Type A + B → X: Toward Systematic Prediction of Reaction Mechanisms. *J. Chem. Theory Comput.* **2011**, *7*, 2335-2345.

(98) Maeda, S.; Ohno, K.; Morokuma, K. Systematic Exploration of the Mechanism of Chemical Reactions: The Global Reaction Route Mapping (GRRM) Strategy Using the ADDF and AFIR Methods. *Phys. Chem. Chem. Phys.* **2013**, *15*, 3683-3701.

(99) Gao, M.; Lyalin, A.; Maeda, S.; Taketsugu, T. Application of Automated Reaction Path Search Methods to a Systematic Search of Single-Bond Activation Pathways Catalyzed by Small Metal Clusters: A Case Study on H–H Activation by Gold. *J. Chem. Theory Comput.* **2014**, *10*, 1623-1630.

(100) Zeng, G.; Maeda, S.; Taketsugu, T.; Sakaki, S. Catalytic Transfer Hydrogenation by a Trivalent Phosphorus Compound: Phosphorus-Ligand Cooperation Pathway or P_{III}/P_V Redox Pathway? *Angew. Chem. Int. Ed.* **2014**, *126*, 4721-4725.

(101) Maeda, S.; Taketsugu, T.; Ohno, K.; Morokuma, K. From Roaming Atoms to Hopping Surfaces: Mapping out Global Reaction Routes in Photochemistry. *J. Am. Chem. Soc.* **2015**, *137*, 3433-3445.

(102) Kresse, G.; Furthmüller, J. Efficient Iterative Schemes for Ab Initio Total-Energy Calculations Using a Plane-Wave Basis Set. *Phys. Rev. B* **1996**, *54*, 11169-11186.

(103) Kresse, G.; Furthmüller, J. Efficiency of Ab-Initio Total Energy Calculations for Metals and Semiconductors Using a Plane-Wave Basis Set. *Comp. Mater. Sci.* **1996**, *6*, 15-50.

(104) Makov, G.; Payne, M. C. Periodic Boundary-Conditions in Ab-Initio Calculations. *Phys. Rev. B* **1995**, *51*, 4014-4022.

(105) Fabris, S.; Vicario, G.; Balducci, G.; de Gironcoli, S.; Baroni, S. Electronic and Atomistic Structures of Clean and Reduced Ceria Surfaces. *J. Phys. Chem. B* **2005**, *109*, 22860-22867.

(106) Dudarev, S. L.; Botton, G. A.; Savrasov, S. Y.; Humphreys, C. J.; Sutton, A. P. Electron-Energy-Loss Spectra and the Structural Stability of Nickel Oxide: An LSDA+U Study. *Phys. Rev. B* **1998**, *57*, 1505-1509.

(107) Bengone, O.; Alouani, M.; Blöchl, P.; Hugel, J. Implementation of the Projector Augmented-Wave LDA+U Method: Application to the Electronic Structure of NiO. *Phys. Rev. B* **2000**, *62*, 16392-16401.

(108) Piccini, G.; Sauer, J. Effect of Anharmonicity on Adsorption Thermodynamics. *J. Chem. Theory Comput.* **2014**, *10*, 2479-2487.

(109) Penschke, C.; Paier, J.; Sauer, J. Oligomeric Vanadium Oxide Species Supported on the CeO_2(111) Surface: Structure and Reactivity Studied by Density Functional Theory. *J. Phys. Chem. C* **2013**, *117*, 5274-5285.

(110) Trovarelli, A. *Catalysis by Ceria and Related Materials*; Imperial College Press: London, **2002**.

(111) Gorte, R. Ceria in Catalysis: From Automotive Applications to the Water-Gas Shift Reaction. *AlChE J.* **2010**, *56*, 1126-1135.

(112) Gandhi, H. S.; Graham, G. W.; McCabe, R. W. Automotive Exhaust Catalysis. *J. Catal.* **2003**, *216*, 433-442.

(113) Steele, B. C. H.; Heinzel, A. Materials for Fuel-Cell Technologies. *Nature* **2001**, *414*, 345-352.

(114) Verhelst, J.; Decroupet, D.; De Vos, D. Catalytic Self-Cleaning Coatings for Thermal Oxidation of Organic Deposits on Glass. *Catal. Sci. Tech.* **2013**, *3*, 1579-1590.

(115) Skorodumova, N. V.; Simak, S. I.; Lundqvist, B. I.; Abrikosov, I. A.; Johansson, B. Quantum Origin of the Oxygen Storage Capability of Ceria. *Phys. Rev. Lett.* **2002**, *89*, 166601.

(116) Duclos, S. J.; Vohra, Y. K.; Ruoff, A. L.; Jayaraman, A.; Espinosa, G. P. High-Pressure X-Ray-Diffraction Study of CeO_2 to 70 GPa and Pressure-Induced Phase-Transformation from the Fluorite Structure. *Phys. Rev. B* **1988**, *38*, 7755-7758.

(117) Gerward, L.; Olsen, J. S.; Petit, L.; Vaitheeswaran, G.; Kanchana, V.; Svane, A. Bulk Modulus of CeO_2 and PrO_2 - an Experimental and Theoretical Study. *J. Alloys Compd.* **2005**, *400*, 56-61.

(118) Mullins, D. R. The Surface Chemistry of Cerium Oxide. *Surf. Sci. Rep.* **2015**, *70*, 42-85.

(119) Nolan, M.; Grigoleit, S.; Sayle, D. C.; Parker, S. C.; Watson, G. W. Density Functional Theory Studies of the Structure and Electronic Structure of Pure and Defective Low Index Surfaces of Ceria. *Surf. Sci.* **2005**, *576*, 217-229.

(120) Skorodumova, N. V.; Baudin, M.; Hermansson, K. Surface Properties of CeO_2 from First Principles. *Phys. Rev. B* **2004**, *69*, 075401.

(121) Marrocchelli, D.; Yildiz, B. First-Principles Assessment of H_2S and H_2O Reaction Mechanisms and the Subsequent Hydrogen Absorption on the CeO_2(111) Surface. *J. Phys. Chem. C* **2012**, *116*, 2411-2424.

(122) Jupille, J.; Thornton, G. *Defects at Oxide Surfaces*; Springer: Heidelberg, **2015**.

(123) Ganduglia-Pirovano, M. V.; Popa, C.; Sauer, J.; Abbott, H. L.; Uhl, A.; Baron, M.; Stacchiola, D.; Bondarchuk, O.; Shaikhutdinov, S.; Freund, H.-J. Role of Ceria in Oxidative Dehydrogenation on Supported Vanadia Catalysts. *J. Am. Chem. Soc.* **2010**, *132*, 2345-2349.

(124) Momma, K.; Izumi, F. VESTA 3 for Three-Dimensional Visualization of Crystal, Volumetric and Morphology Data. *J. Appl. Crystallogr.* **2011**, *44*, 1272-1276.

(125) Pol, A.; Barends, T. R. M.; Dietl, A.; Khadem, A. F.; Eygensteyn, J.; Jetten, M. S. M.; Op den Camp, H. J. M. Rare Earth Metals Are Essential for Methanotrophic Life in Volcanic Mudpots. *Environ. Microbiol.* **2014**, *16*, 255-264.

(126) Ganduglia-Pirovano, M. V.; Da Silva, J. L. F.; Sauer, J. Density Functional Calculations of the Structure of near-Surface Oxygen Vacancies and Electron Ocalization on CeO_2(111). *Phys. Rev. Lett.* **2009**, *102*, 026101.

(127) Yang, C.; Yin, L.-L.; Bebensee, F.; Buchholz, M.; Sezen, H.; Heissler, S.; Chen, J.; Nefedov, A.; Idriss, H.; Gong, X.-Q.; Wöll, C. Chemical Activity of Oxygen Vacancies on Ceria: A Combined Experimental and Theoretical Study on CeO_2(111). *Phys. Chem. Chem. Phys.* **2014**, *16*, 24165-24168.

(128) Nolan, M.; Fearon, J. E.; Watson, G. W. Oxygen Vacancy Formation and Migration in Ceria. *Solid State Ion.* **2006**, *177*, 3069-3074.

(129) Nolan, M. Enhanced Oxygen Vacancy Formation in Ceria (111) and (110) Surfaces Doped with Divalent Cations. *J. Mater. Chem.* **2011**, *21*, 9160-9168.

(130) Pan, Y.; Nilius, N.; Freund, H.-J.; Paier, J.; Penschke, C.; Sauer, J. Titration of Ce^{3+} Ions in the Ceo_2(111) Surface by Au Adatoms. *Phys. Rev. Lett.* **2013**, *111*, 206101.

(131) Shahed, S. M. F.; Sainoo, Y.; Komeda, T. Scanning Tunneling Microscope Study of Surface Morphology Variation of CeO_2(111) with Changing Annealing Condition. *Jpn. J. Appl. Phys.* **2011**, *50*, 08LB05.

(132) Torbrügge, S.; Cranney, M.; Reichling, M. Morphology of Step Structures on CeO_2(111). *Appl. Phys. Lett.* **2008**, *93*, 073112.

(133) Nilius, N.; Kozlov, S. M.; Jerratsch, J. F.; Baron, M.; Shao, X.; Vines, F.; Shaikhutdinov, S.; Neyman, K. M.; Freund, H. J. Formation of One-Dimensional Electronic States Along the Step Edges of CeO_2(111). *ACS Nano* **2012**, *6*, 1126-1133.

(134) Kozlov, S. M.; Vines, F.; Nilius, N.; Shaikhutdinov, S.; Neyman, K. M. Absolute Surface Step Energies: Accurate Theoretical Methods Applied to Ceria Nanoislands. *J. Phys. Chem. Lett.* **2012**, *3*, 1956-1961.

(135) Kozlov, S. M.; Neyman, K. M. O Vacancies on Steps on the CeO_2(111) Surface. *Phys. Chem. Chem. Phys.* **2014**, *16*, 7823-7829.

(136) Overbury, S. H.; Huntley, D. R.; Mullins, D. R.; Ailey, K. S.; Radulovic, P. V. Surface Studies of Model Supported Catalysts: NO Adsorption on Rh/CeO_2(001). *J. Vac. Sci. Technol. A* **1997**, *15*, 1647-1652.

(137) Herman, G. S. Surface Structure Determination of CeO_2(001) by Angle-Resolved Mass Spectroscopy of Recoiled Ions. *Phys. Rev. B* **1999**, *59*, 14899-14902.

(138) Nörenberg, H.; Harding, J. H. The Surface Structure of CeO_2(001) Single Crystals Studied by Elevated Temperature STM. *Surf. Sci.* **2001**, *477*, 17-24.

(139) Yang, F.; Choi, Y.; Agnoli, S.; Liu, P.; Stacchiola, D.; Hrbek, J.; Rodriguez, J. A. $CeO_2 \leftrightarrow CuO_x$ Interactions and the Controlled Assembly of CeO_2(111) and CeO_2(100) Nanoparticles on an Oxidized Cu(111) Substrate. *J. Phys. Chem. C* **2011**, *115*, 23062-23066.

(140) Stetsovych, O.; Beran, J.; Dvořák, F.; Mašek, K.; Mysliveček, J.; Matolín, V. Polarity Driven Morphology of CeO_2(100) Islands on Cu(111). *Appl. Surf. Sci.* **2013**, *285, Part B*, 766-771.

(141) Lin, Y.; Wu, Z.; Wen, J.; Poeppelmeier, K. R.; Marks, L. D. Imaging the Atomic Surface Structures of CeO_2 Nanoparticles. *Nano Lett.* **2014**, *14*, 191-196.

(142) Pan, Y.; Nilius, N.; Stiehler, C.; Freund, H.-J.; Goniakowski, J.; Noguera, C. Ceria Nanocrystals Exposing Wide (100) Facets: Structure and Polarity Compensation. *Adv. Mater. Interfaces* **2014**, *1*, 1400404.

(143) Rohr, F.; Wirth, K.; Libuda, J.; Cappus, D.; Baumer, M.; Freund, H. J. Hydroxyl Driven Reconstruction of the Polar NiO(111) Surface. *Surf. Sci.* **1994**, *315*, L977-L982.

(144) Goniakowski, J.; Finocchi, F.; Noguera, C. Polarity of Oxide Surfaces and Nanostructures. *Rep. Prog. Phys.* **2008**, *71*, 016501.

(145) Tasker, P. W. The Stability of Ionic Crystal Surfaces. *J. Phys. C: Solid State Phys.* **1979**, *12*, 4977.

(146) Baron, M.; Abbott, H.; Bondarchuk, O.; Stacchiola, D.; Uhl, A.; Shaikhutdinov, S.; Freund, H.-J.; Popa, C.; Ganduglia-Pirovano, M. V.; Sauer, J. Resolving the Atomic Structure of Vanadia Monolayer Catalysts: Monomers, Trimers, and Oligomers on Ceria. *Angew. Chem. Int. Edit.* **2009**, *48*, 8006-8009.

(147) Abbott, H. L.; Uhl, A.; Baron, M.; Lei, Y.; Meyer, R. J.; Stacchiola, D. J.; Bondarchuk, O.; Shaikhutdinov, S.; Freund, H. J. Relating Methanol Oxidation to the Structure of Ceria-Supported Vanadia Monolayer Catalysts. *J. Catal.* **2010**, *272*, 82-91.

(148) Beck, B.; Harth, M.; Hamilton, N. G.; Carrero, C.; Uhlrich, J. J.; Trunschke, A.; Shaikhutdinov, S.; Schubert, H.; Freund, H.-J.; Schlögl, R.; Sauer, J.; Schomäcker, R. Partial Oxidation of Ethanol on Vanadia Catalysts on Supporting Oxides with Different Redox Properties Compared to Propane. *J. Catal.* **2012**, *296*, 120-131.

(149) McQuarters, A. B.; Wolf, M. W.; Hunt, A. P.; Lehnert, N. 1958-2014: After 56 Years of Research, Cytochrome P450 Reactivity Is Finally Explained. *Angew. Chem. Int. Edit.* **2014**, *53*, 4750-4752.

(150) Vohs, J. M. Site Requirements for the Adsorption and Reaction of Oxygenates on Metal Oxide Surfaces. *Chem. Rev.* **2012**, *113*, 4136-4163.

(151) Popa, C.; Ganduglia-Pirovano, M. V.; Sauer, J. Periodic Density Functional Theory Study of VO_n Species Supported on the CeO_2(111) Surface. *J. Phys. Chem. C* **2011**, *115*, 7399-7410.

(152) Popa, C.; Ganduglia-Pirovano, M. V.; Sauer, J. Correction to "Periodic Density Functional Theory Study of VO_n Species Supported on the CeO_2(111) Surface". *J. Phys. Chem. C* **2012**, *116*, 18572-18573.

(153) Mei, D.; Deskins, N. A.; Dupuis, M.; Ge, Q. Methanol Adsorption on the Clean CeO_2(111) Surface: A Density Functional Theory Study. *J. Phys. Chem. C* **2007**, *111*, 10514-10522.

(154) Beste, A.; Mullins, D. R.; Overbury, S. H.; Harrison, R. J. Adsorption and Dissociation of Methanol on the Fully Oxidized and Partially Reduced (111) Cerium Oxide Surface: Dependence on the Configuration of the Cerium 4*f* Electrons. *Surf. Sci.* **2008**, *602*, 162-175.

(155) Li, C.; Domen, K.; Maruya, K.-i.; Onishi, T. Spectroscopic Identification of Adsorbed Species Derived from Adsorption and Decomposition of Formic Acid, Methanol, and Formaldehyde on Cerium Oxide. *J. Catal.* **1990**, *125*, 445-455.

(156) Badri, A.; Binet, C.; Lavalley, J. C. Use of Methanol as an IR Molecular Probe to Study the Surface of Polycrystalline Ceria. *J. Chem. Soc.-Faraday Trans.* **1997**, *93*, 1159-1168.

(157) Wu, Z.; Li, M.; Mullins, D. R.; Overbury, S. H. Probing the Surface Sites of CeO_2 Nanocrystals with Well-Defined Surface Planes Via Methanol Adsorption and Desorption. *ACS Catal.* **2012**, *2*, 2224-2234.

(158) Siokou, A.; Nix, R. M. Interaction of Methanol with Well-Defined Ceria Surfaces: Reflection/Absorption Infrared Spectroscopy, X-Ray Photoelectron Spectroscopy, and Temperature-Programmed Desorption Study. *J. Phys. Chem. B* **1999**, *103*, 6984-6997.

(159) Namai, Y.; Fukui, K.; Iwasawa, Y. The Dynamic Behaviour of CH_3OH and NO_2 Adsorbed on CeO_2(111) Studied by Noncontact Atomic Force Microscopy. *Nanotechnology* **2004**, *15*, S49-S54.

(160) Mullins, D. R.; Robbins, M. D.; Zhou, J. Adsorption and Reaction of Methanol on Thin-Film Cerium Oxide. *Surf. Sci.* **2006**, *600*, 1547-1558.

(161) Albrecht, P. M.; Mullins, D. R. Adsorption and Reaction of Methanol over CeO_x(100) Thin Films. *Langmuir* **2013**, *29*, 4559-4567.

(162) Uhlrich, J.; Yang, B.; Shaikhutdinov, S. Methanol Reactivity on Silica-Supported Ceria Nanoparticles. *Top. Catal.* **2014**, *57*, 1229–1235.

(163) Pauling, L. The Principles Determining the Structure of Complex Ionic Crystals. *J. Am. Chem. Soc.* **1929**, *51*, 1010-1026.

(164) Badlani, M.; Wachs, I. E. Methanol: A "Smart" Chemical Probe Molecule. *Catal. Lett.* **2001**, *75*, 137-149.

(165) Ferrizz, R. M.; Wong, G. S.; Egami, T.; Vohs, J. M. Structure Sensitivity of the Reaction of Methanol on Ceria. *Langmuir* **2001**, *17*, 2464-2470.

(166) Feng, T.; Vohs, J. M. A Tpd Study of the Partial Oxidation of Methanol to Formaldehyde on CeO_2-Supported Vanadium Oxide. *J. Catal.* **2004**, *221*, 619-629.

(167) Zhao, Y.; Gonzalez-Garcia, N.; Truhlar, D. G. Benchmark Database of Barrier Heights for Heavy Atom Transfer, Nucleophilic Substitution, Association, and Unimolecular Reactions and Its Use to Test Theoretical Methods. *J. Phys. Chem. A* **2005**, *109*, 2012-2018.

(168) Teng, B. T.; Jiang, S. Y.; Yang, Z. X.; Luo, M. F.; Lan, Y. Z. A Density Functional Theory Study of Formaldehyde Adsorption and Oxidation on CeO_2(111) Surface. *Surf. Sci.* **2010**, *604*, 68-78.

(169) Capdevila-Cortada, M.; García-Melchor, M.; López, N. Unraveling the Structure Sensitivity in Methanol Conversion on CeO_2: A DFT+*U* Study. *J. Catal.* **2015**, *327*, 58-64.

(170) Freund, H. J.; Roberts, M. W. Surface Chemistry of Carbon Dioxide. *Surf. Sci. Rep.* **1996**, *25*, 225-273.

(171) Benkovic, S. J.; Hammes-Schiffer, S. A Perspective on Enzyme Catalysis. *Science* **2003**, *301*, 1196-1202.

(172) Redhead, P. A. Thermal Desorption of Gases. *Vacuum* **1962**, *12*, 203-211.

(173) Chen, B.; Ma, Y.; Ding, L.; Xu, L.; Wu, Z.; Yuan, Q.; Huang, W. Reactivity of Hydroxyls and Water on a CeO_2(111) Thin Film Surface: The Role of Oxygen Vacancy. *J. Phys. Chem. C* **2013**, *117*, 5800-5810.

(174) Henderson, M. A.; Perkins, C. L.; Engelhard, M. H.; Thevuthasan, S.; Peden, C. H. F. Redox Properties of Water on the Oxidized and Reduced Surfaces of CeO_2(111). *Surf. Sci.* **2003**, *526*, 1-18.

(175) Mullins, D. R.; Albrecht, P. M.; Chen, T.-L.; Calaza, F. C.; Biegalski, M. D.; Christen, H. M.; Overbury, S. H. Water Dissociation on CeO_2(100) and CeO_2(111) Thin Films. *J. Phys. Chem. C* **2012**, *116*, 19419-19428.

(176) Matolin, V.; Matolinova, I.; Dvorak, F.; Johanek, V.; Myslivecek, J.; Prince, K. C.; Skala, T.; Stetsovych, O.; Tsud, N.; Vaclavu, M.; Smid, B. Water Interaction with CeO_2(111)/Cu(111) Model Catalyst Surface. *Catal. Today* **2012**, *181*, 124-132.

(177) Campbell, C. T.; Sellers, J. R. V. Enthalpies and Entropies of Adsorption on Well-Defined Oxide Surfaces: Experimental Measurements. *Chem. Rev.* **2013**, *113*, 4106-4135.

(178) Gritschneder, S.; Namai, Y.; Iwasawa, Y.; Reichling, M. Structural Features of CeO_2(111) Revealed by Dynamic SFM. *Nanotechnology* **2005**, *16*, S41-S48.

(179) Watkins, M. B.; Foster, A. S.; Shluger, A. L. Hydrogen Cycle on CeO_2 (111) Surfaces: Density Functional Theory Calculations. *J. Phys. Chem. C* **2007**, *111*, 15337-15341.

(180) Chen, H. T.; Choi, Y. M.; Liu, M. L.; Lin, M. C. A Theoretical Study of Surface Reduction Mechanisms of CeO_2 (111) and (110) by H_2. *ChemPhysChem* **2007**, *8*, 849-855.

(181) Fronzi, M.; Piccinin, S.; Delley, B.; Traversa, E.; Stampfl, C. Water Adsorption on the Stoichiometric and Reduced CeO_2(111) Surface: A First-Principles Investigation. *Phys. Chem. Chem. Phys.* **2009**, *11*, 9188-9199.

(182) Yang, Z.; Wang, Q.; Wei, S.; Ma, D.; Sun, Q. The Effect of Environment on the Reaction of Water on the Ceria(111) Surface: A DFT+U Study. *J. Phys. Chem. C* **2010**, *114*, 14891-14899.

(183) Fernández-Torre, D.; Kosmider, K.; Carrasco, J.; Ganduglia-Pirovano, M. V.; Pérez, R. Insight into the Adsorption of Water on the Clean CeO_2(111) Surface with Van Der Waals and Hybrid Density Functionals. *J. Phys. Chem. C* **2012**, *116*, 13584-13593.

(184) Molinari, M.; Parker, S. C.; Sayle, D. C.; Islam, M. S. Water Adsorption and Its Effect on the Stability of Low Index Stoichiometric and Reduced Surfaces of Ceria. *J. Phys. Chem. C* **2012**, *116*, 7073-7082.

(185) Carrasco, J.; Illas, F.; Lopez, N. Dynamic Ion Pairs in the Adsorption of Isolated Water Molecules on Alkaline-Earth Oxide (001) Surfaces. *Phys. Rev. Lett.* **2008**, *100*, 016101.

(186) Dementyev, P.; Dostert, K.-H.; Ivars-Barceló, F.; O'Brien, C. P.; Mirabella, F.; Schauermann, S.; Li, X.; Paier, J.; Sauer, J.; Freund, H.-J. Water Interaction with Iron Oxides. *Angew. Chem. Int. Ed.* **2015**, 54, 13942-13946.

(187) Meyer, B.; Marx, D.; Dulub, O.; Diebold, U.; Kunat, M.; Langenberg, D.; Wöll, C. Partial Dissociation of Water Leads to Stable Superstructures on the Surface of Zinc Oxide. *Angew. Chem. Int. Ed.* **2004**, *43*, 6641-6645.

(188) Algara-Siller, G.; Lehtinen, O.; Wang, F. C.; Nair, R. R.; Kaiser, U.; Wu, H. A.; Geim, A. K.; Grigorieva, I. V. Square Ice in Graphene Nanocapillaries. *Nature* **2015**, *519*, 443-445.

(189) Fernández-Torre, D.; Carrasco, J.; Ganduglia-Pirovano, M. V.; Pérez, R. Hydrogen Activation, Diffusion, and Clustering on CeO_2(111): A DFT+U Study. *J. Chem. Phys.* **2014**, *141*, 014703.

(190) García-Melchor, M.; López, N. Homolytic Products from Heterolytic Paths in H_2 Dissociation on Metal Oxides: The Example of CeO_2. *J. Phys. Chem. C* **2014**, *118*, 10921-10926.

(191) Negreiros, F. R.; Camellone, M. F.; Fabris, S. Effects of Thermal Fluctuations on the Hydroxylation and Reduction of Ceria Surfaces by Molecular H_2. *J. Phys. Chem. C* **2015**, *119*, 21567-21573.

(192) Shapovalov, V.; Fievez, T.; Bell, A. T. A Theoretical Study of Methanol Oxidation Catalyzed by Isolated Vanadia Clusters Supported on the (101) Surface of Anatase. *J. Phys. Chem. C* **2012**, *116*, 18728-18735.

7. ACKNOWLEDGEMENTS

I would like to thank Prof. Dr. Joachim Sauer for giving me the opportunity to work in his group. His feedback and the freedom to pursue my own research interests were highly appreciated. I also want to thank Dr. Joachim Paier for his support and for teaching me a great deal about solid state physics. Last but not least, I thank all the group members for helping me in different phases of this work.

This work has been supported by the "Fonds der Chemischen Industrie" as well as by grants for computer time at the high-performance computer centers HLRN (North-German Supercomputing Alliance in Berlin and Hannover). COST action CM1104 is gratefully acknowledged.

8. SELBSTSTÄNDIGKEITSERKLÄRUNG

Hiermit erkläre ich, dass ich die vorliegende Dissertation selbstständig und nur unter Verwendung der angegebenen Hilfsmittel und Quellen angefertigt habe.

Thomas E. Kropp